negative control, an antibody to COX-IV, a mitochondrial membrane protein, was used. The precipitates were subjected to SDS-PAGE, followed by Western blotting with AB.H10 and a monoclonal antibody to APP/Aβ (6E10; Signet Laboratories, Dedham, MA), as described previously (Nishitsuji et al., 2009).

^{14}C-Labeled Cholesterol/MβCD Complex

^{14}C-labeled cholesterol/MβCD complex was prepared using ^{14}C-cholesterol (Amersham Biosciences, Piscataway, NJ) essentially as described previously (Klein et al., 1995). In brief, 25 μCi (0.195 mg) of ^{14}C-cholesterol and 2.805 mg of nonlabeled cholesterol (Sigma) were mixed with 100 mg MβCD (Sigma) in 0.3 ml water and stirred for 60 min at room temperature. The clear solution was frozen at −80°C, and the solvent was evaporated under a vacuum. The dried complex was resuspended in 7.75 ml of DMEM (Sigma) to a cholesterol concentration of 1 mM. The calculated specific activity of the resulting complex was 3.33 mCi/mmol cholesterol.

^{14}C-Labeled Reconstituted Lipoproteins

^{14}C-labeled reconstituted lipoproteins were prepared using ^{14}C-cholesterol essentially as described previously (Tajima et al., 1983). In brief, 50 μCi (0.39 mg) of ^{14}C-cholesterol, 3.51 mg of nonlabeled cholesterol, 11.52 mg of cholesteryl oleate (Sigma), 18.59 mg of phosphatidylcholine (Sigma), and 3.16 mg of glyceryl trioleate (Sigma) were mixed in 3 ml of PBS, and sonicated 10 times for 3 min each with 1-min intervals at 12 W while being cooled in an ice bath. The proportion of lipids in this mixture reflects that in plasma HDL. The solution was centrifuged at 410,000*g* for 2 hr at 4°C. The floating fraction (about 1 ml) at the top of the solution was recovered as lipoprotein-like particles. The radioactive concentration of the particle solution was 55,000 dpm/μl. An aliquot of the solution was incubated with 10 μM Aβ40 in 5.4 ml of PBS for 30 min at room temperature. The ratio of Aβ to lipid particles in this mixture was 5:1, which reflects that of apoE to HDL particles in plasma. After being concentrated using a 50K-cut membrane device (Centricon YM-50; Millipore, Billerica, MA), the solution was diluted to 100,000 dpm/μl. ^{14}C-labeled control lipid particles without Aβ were also prepared. The Aβ/lipid particles complex prepared by the same method, except for use of nonlabeled cholesterol instead of ^{14}C-cholesterol, was examined for Aβ by immunoelectron microscopy with an anti-Aβ antibody, as described below. The resultant lipid particles were approximately 30–60 nm in diameter and thus larger than plasma HDL and similar to LDL-VLDL in size.

Cholesterol Efflux From Cells

Cholesterol loading onto cells was performed with 1 mM ^{14}C-labeled cholesterol/MβCD complex in serum-free DMEM at 4°C for 1 hr. At this temperature, cellular activities presumably declined, and Aβ production was probably inhibited. After cholesterol loading, the culture media were replaced with serum-free DMEM, and the cells were further incubated at 37°C for 1 hr to allow cholesterol efflux. The culture media and cells were harvested separately, and their radioactivity was counted with a liquid scintillation counter. In some experiments, the conditioned media were fractionated to VLDL, LDL, HDL, and VHDL fractions by sequential ultracentrifugation according to the method of Hatch (1968), with minor modifications. In brief, conditioned media were supplemented with 0.1% EDTA and 0.01% NaN_3, and 2 ml of the solution was overlaid with 1 ml of NaCl solution (d = 1.006) and centrifuged at 80,000 rpm for 4 hr at 16°C using a himac CS120 ultracentrifuge and a RP80AT rotor (Hitachi Koki Co., Ltd., Tokyo, Japan). The upper phase (1 ml) was harvested as the VLDL (0.96 < d < 1.006) fraction. The lower phase (1.8 ml) was mixed with 0.9 ml of NaCl-NaBr solution (d = 1.182) to make the relative density 1.063. Then, the solution was overlaid with 500 μl of NaCl-NaBr solution (d = 1.063) and centrifuged at 80,000 rpm for 5 hr. The upper phase (1 ml) was harvested as the LDL (1.006 < d < 1.063) fraction. The lower phase (2 ml) was mixed with 1 ml of NaCl-NaBr solution (d = 1.478) to make the relative density 1.21, overlaid with 200 μl of NaCl-NaBr solution (d = 1.21), and centrifuged at 80,000 rpm for 10 hr. The upper phase (1 ml) was harvested as the HDL (1.063 < d < 1.21) fraction. The lower phase (2.2 ml) was mixed with 386 μl of NaCl-NaBr solution (d = 1.478) to make the relative density 1.25, overlaid with 700 μl of NaCl-NaBr solution (d = 1.25), and centrifuged at 80,000 rpm for 4.5 hr. Finally, the upper phase (1 ml) was harvested as the VHDL (1.21 < d < 1.25) fraction. The radioactivity in each fraction was counted.

Cholesterol Efflux From the Brain

Twelve-month-old APP knockout mice were anesthetized with pentobarbital and placed on a stereotaxic apparatus. One microliter (100,000 dpm) of the ^{14}C-labeled reconstituted lipoproteins with or without Aβ was injected into the cerebral ventricle over 1 min using a Hamilton syringe. The syringe was left in place for 10 min to avoid regurgitation of the injectate. 10 or 60 min after injection, the mice were dissected into liver, spleen, kidney, heart, and lung, and then decapitated to harvest the brain. The collected tissues were homogenized in a Polytron PT3100 homogenizer (Kinematica, Bohemia, NY) in 9 vol of water, and 200 μl of the homogenate was mixed with 3 ml of water and added to 10 ml of liquid scintillation cocktail Insta-Gel Plus (PerkinElmer, Waltham, MA). The radioactivity in each sample was counted. All animal experiments were performed in accordance with the Guide for Animal Experimentation, Osaka City University.

Immunoelectron Microscopy

Samples were absorbed onto 200-mesh carbon-coated nickel grids (Stork Veco B.V., Eerbeek, The Netherlands). The grids were blocked with 1%BSA/PBS for 10 min and incubated with an anti-Aβ polyclonal antibody (β001; Lippa et al., 1999) for 1 hr. followed by 10 nm gold-labeled second antibody (AuroProbe EM GAR G10; Amersham) for 1 hr. After being washed with PBS and water, the specimens were negatively stained with 2% phosphotungstate (TAAB Laboratories Equipment Ltd., Berks, United Kingdom) and viewed

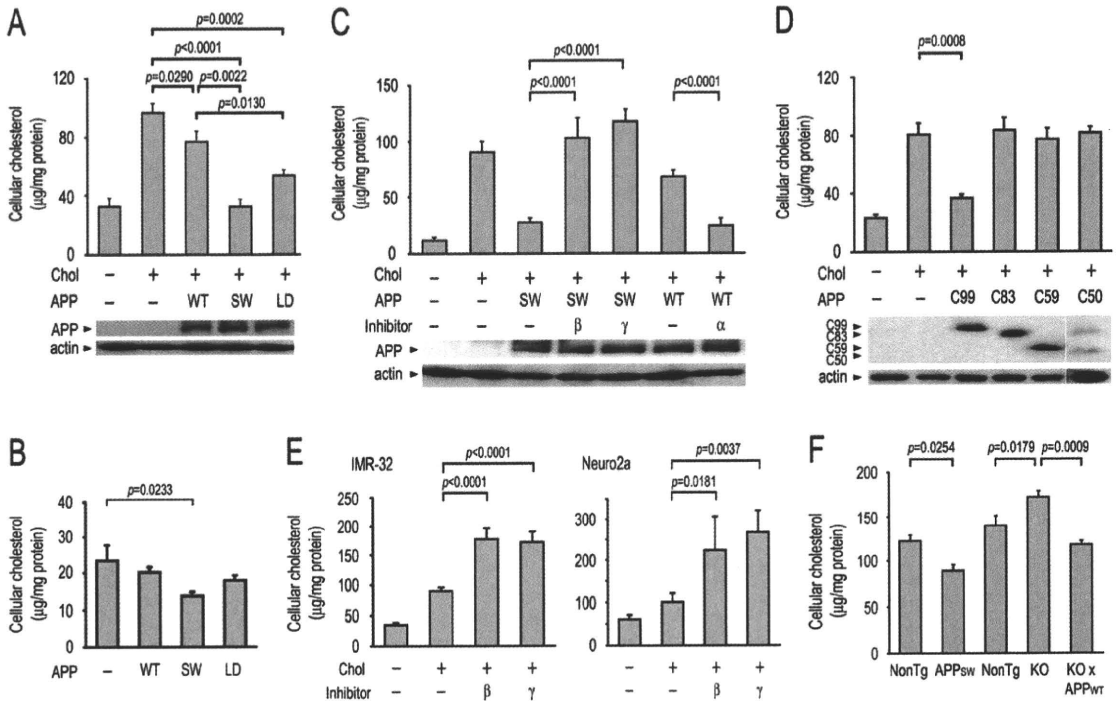

Fig. 1. Aβ regulates cellular cholesterol levels. **A:** APP-expressing HEK293 cells exhibited lower levels of cellular cholesterol than mock-trasfected cells after cholesterol loading. APP_{SW} and APP_{LD} exhibited more potent effects than APP_{WT}. **B:** Cholesterol-lowering effects of APP expression were also observed under physiological conditions without cholesterol loading. **C:** Inhibition of Aβ production with β- and γ-secretase inhibitors attenuated the effect of APP expression, whereas enhancement of Aβ production with α-secretase inhibitor exhibited the opposite effect. **D:** C99, but not C83, C59, or C50, exhibited an effect similar to that of APP. **E:** Aβ-mediated regulation of cellular cholesterol was also observed in nontransfected neuronal cells. Inhibition of Aβ production with β- and γ-secretase inhibitors increased cellular cholesterol levels in both IMR-32 and Neuro2a cells. **F:** APP_{SW} transgenic (Tg2576) mice (6 months) exhibited lower, whereas APP knockout mice (12 months) exhibited higher cellular cholesterol in the brain than the age-matched control mice. Cross-breeding of APP knockout mice with APP_{WT} transgenic mice resulted in lower cellular cholesterol levels. NonTg, nontransgenic littermates of the Tg2576 mice or nontransgenic wild-type mice; KO, APP knockout mice. Comparison between APP_{SW} and NonTg was performed using the unpaired Student's *t*-test, whereas those among KO, NonTg, and KO × APP_{WT} were performed using Fisher's PLSD test following ANOVA. All columns and bars represent the mean ± SEM (A–E, n = 3; F, n = 4).

under a JEM-1200EX2 electron microscope (JEOL Ltd., Akishima, Japan).

Statistical Analysis

All values obtained are expressed as the mean ± SEM. Comparisons of means between two groups were performed using the unpaired Student's *t*-test, whereas those among multiple groups were performed using Fisher's PLSD test following ANOVA.

RESULTS

Aβ Regulates Cellular Cholesterol Levels

We initially examined the effect of Aβ production on cellular cholesterol levels in vitro. HEK293 cells transfected with APP were cholesterol-loaded by incubation with cholesterol/ MβCD complex. Compared with mock-transfected cells, APP-expressing cells exhibited significantly lower levels of cellular cholesterol (Fig. 1A). APP with the Swedish mutation (K670N/M671L; APP_{SW}), which increases total Aβ production (Table I), and that with the London mutation (V717I; APP_{LD}), which selectively enhances Aβ42 production (Table I), were more effective than wild-type APP (APP_{WT}). The cholesterol-lowering effect of APP expression was also observed under physiological conditions without cholesterol loading (Fig. 1B). When Aβ production was inhibited by β-secretase inhibitor II or γ-secretase inhibitor L-685,458 (Table I), the effect of APP expression on cellular cholesterol was attenuated (Fig. 1C). In contrast, in the presence of α-secretase inhibitor TAPI-I, which leads to increased Aβ production (Table I), the effect of APP was enhanced (Fig. 1C). Thus, cellular cholesterol level was shown to be regulated depending on Aβ (particularly Aβ42) production but not expression of APP holoprotein. A cholesterol-lowering effect was also displayed by C99, an APP carboxyl-terminal fragment that can produce Aβ (Table I), but not by C83, another

TABLE I. Aβ Secretion From Cells

	Aβ1–40 (pg/ml)	Aβ1–42 (pg/ml)
HEK293 cells		
Mock	33 ± 2	0 ± 0
APP_{WT}	258 ± 25	14 ± 0
+ α-Inhibitor	829 ± 14	32 ± 1
APP_{SW}	4,078 ± 1,420	137 ± 21
+ β-Inhibitor	26 ± 3	2 ± 1
+ γ-Inhibitor	53 ± 15	ND
APP_{LD}	161 ± 14	31 ± 2
C99	2,142 ± 428	106 ± 1
C83	58 ± 3	3 ± 1
C59	75 ± 4	3 ± 1
IMR-32 cells		
Control	159 ± 3	10 ± 0
+ β-Inhibitor	46 ± 1	6 ± 1
+ γ-Inhibitor	31 ± 3	4 ± 1
HEK293 cells		
APP_{SW}	175 ± 7	12 ± 1
+ Cholesterol	261 ± 15	14 ± 1

*HEK293 cells were transfected with APP constructs and cultured in serum-free medium for 1 day in the presence or absence of secretase inhibitors. Aβ concentrations in culture media were determined by ELISA. IMR-32 and Neuro-2a cells were also cultured in serum-free medium for 1 day in the presence or absence of secretase inhibitors. Aβ concentrations of IMR-32 cells are shown, but those of Neuro-2a cells could not be measured because the ELISA kits used are for human Aβ alone and not mouse Aβ. In another experiment, HEK293 cells transfected with APP_{SW} were loaded with cholesterol in serum-free medium for 1 hr, and culture media were immediately removed without further incubation to determine Aβ concentrations. Values are means ± SEM for triplicate transfections. ND, not detected.

APP carboxyl-terminal fragment that produces p3 peptide instead of Aβ, or APP intracellular domains (AICDs) such as C59 and C50 (Fig. 1D). These findings exclude the possibility of contribution of p3 peptide and AICD to the cholesterol-lowering effect. Aβ-mediated regulation of cellular cholesterol was also observed in two types of neuronal cells, IMR-32 and Neuro2a, both of which were not transfected with APP but produce endogenous human and mouse Aβ, respectively. Inhibition of Aβ production by β- and γ-secretase inhibitors induced higher levels of cellular cholesterol in these cells (Fig. 1E).

APP Expression Influences Cellular Cholesterol Levels in the Brain

If Aβ participates in the regulation of cellular cholesterol, APP expression levels should influence cellular cholesterol levels in vivo. Thus we examined cellular cholesterol levels in the brains of APP_{SW} transgenic (Tg2576) mice at 6 months and APP knockout mice at 12 months of age. The Tg2576 mice are known to possess no amyloid pathology at this age. Cellular cholesterol levels in Tg2576 mice were lower than those in age-matched nontransgenic littermates, whereas those in APP knockout mice were higher than those in nontransgenic wild-type mice (Fig. 1F). Importantly, the high cholesterol levels in APP knockout mice were reversed to levels beneath those in wild-type mice by cross-breeding with APP_{WT} transgenic mice. This suggests that APP is involved in physiological regulation of cellular cholesterol probably through Aβ production.

Aβ Promotes Cholesterol Efflux From Cells

We assumed that Aβ reduced cellular cholesterol levels by enhancing cholesterol efflux from cells probably via its apolipoprotein-like function. Thus we examined efflux of cellular cholesterol in APP-expressing cells. For this purpose, we prepared radiolabeled cholesterol/MβCD complex using ^{14}C-cholesterols and loaded it onto HEK293 cells. Cholesterol efflux was measured by counting radioactivities of the culture media and cells. In mock-transfected cells, approximately 13% of the loaded ^{14}C-cholesterol was excreted into the media, whereas excretion increased up to 39% in APPsw-expressing cells (Fig. 2A). In parallel with the cholesterol efflux, increased Aβ secretion from cells was observed (Table I). When Aβ production was inhibited by γ-secretase inhibitor, cholesterol efflux decreased to levels in mock-transfected cells (Fig. 2A). Aβ-mediated cholesterol efflux was also observed in nontransfected IMR-32 cells, in which β- and γ-secretase inhibitors attenuated the efflux again. (Fig. 2B).

Aβ Assembles Lipoprotein-Like Particles During Its Secretion

Cholesterol efflux from cells is usually accompanied by lipoprotein formation (Yokoyama, 2005). To determine whether lipoprotein formation occurs in Aβ-mediated cholesterol efflux and which lipoproteins are formed, if any, we fractionated conditioned media of APP_{SW}-expressing HEK293 cells by sequential ultracentrifugation into the VLDL ($0.96 < d < 1.006$), LDL ($1.006 < d < 1.063$), HDL ($1.063 < d < 1.21$), and VHDL ($1.21 < d < 1.25$) fractions. Approximately 50% of ^{14}C-cholesterol in the media was collected in the HDL fraction (Fig. 2C). With immunoelectron microscopy, the HDL fraction was found to contain many Aβ-positive lipoprotein-like particles with diameters of 10–50 nm, ranging from HDL to VLDL in size, whereas very few lipoprotein-like particles were observed in the HDL fraction in the presence of γ-secretase inhibitor (Fig. 2D). These findings indicate that Aβ promoted cholesterol efflux by assembling lipoprotein-like particles with cellular cholesterol during its secretion. It is unlikely that these particles were formed after Aβ secretion by extracellular Aβ to pull out cholesterol from the plasma membrane (Michikawa et al., 2001), insofar as addition of synthetic Aβ peptide to culture medium after cholesterol loading did not reduce cellular cholesterol levels (Fig. 2E). Furthermore, the possibility was ruled out that Aβ secreted from cells bound to cholesterol in the media to prevent their cellular uptake (Yao and Papadopoulos, 2002), because the presence of Aβ in

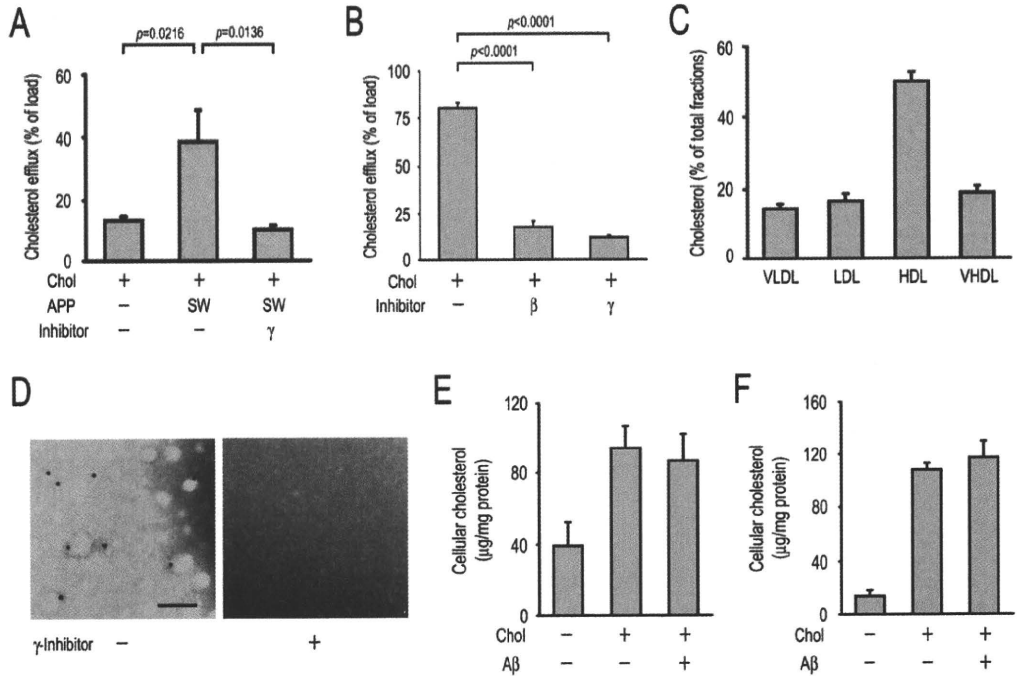

Fig. 2. Aβ promotes cholesterol efflux from cells by assembling lipoprotein-like particles during its secretion. **A:** APP_{SW}-expressing HEK293 cells exhibited higher cholesterol efflux into medium than mock-transfected cells. Inhibition of Aβ production with γ-secretase inhibitor attenuated the cholesterol efflux. **B:** Cholesterol efflux and its inhibition by β- and γ-secretase inhibitors were also observed in nontransfected IMR-32 cells. **C:** Conditioned media of APP_{SW}-expressing HEK293 cells were fractionated by sequential ultracentrifugation. Approximately 50% of cholesterol in the media was collected in the HDL fraction. **D:** The HDL fraction contained many Aβ-positive lipoprotein-like particles with diameters of 10–50 nm. In contrast, very few lipoprotein-like particles were observed in the HDL fraction in the presence of γ-secretase inhibitor. Aβ was probed with 10-nm gold particles. **E:** Addition of Aβ to culture medium after cholesterol loading did not affect cellular cholesterol levels. **F:** The presence of Aβ in culture medium during cholesterol loading did not affect cholesterol levels loaded into cells. All columns and bars represent the mean ± SEM (n = 3). Scale bar = 100 nm.

culture medium during cholesterol loading did not affect cholesterol levels loaded onto cells (Fig. 2F).

Aβ-Induced Cholesterol Efflux Is Mediated by ABCA1

It has been proposed that ABCA1 plays a key role in apolipoprotein-mediated cholesterol efflux from cells (Yokoyama, 2005). ABCA1, a transmembrane protein, interacts with extracellular lipid-poor apolipoproteins, such as apoA-I and apoE, and transports cellular cholesterol to those proteins. To examine whether Aβ-mediated cholesterol efflux depends on ABCA1, we knocked down ABCA1 of IMR-32 cells with a short interfering RNA (siRNA). This treatment resulted in increased cellular cholesterol levels (Fig. 3A) and decreased cholesterol efflux from cells (Fig. 3B). In addition, direct interaction between ABCA1 and APP/Aβ was demonstrated in nontransfected IMR-32 and transfected HEK293 cells by immunoprecipitation (Fig. 3C). Notably, their interaction was apparently promoted by cholesterol loading onto cells. APP and Aβ coprecipitated with ABCA1 increased up to 254% ($P = 0.0243$ vs. without cholesterol) and 206% ($P = 0.0483$), respectively, whereas ABCA1 coprecipitated with APP increased up to 333% ($P = 0.0049$) by cholesterol loading (n = 3 for each group). These findings indicate that Aβ-mediated cholesterol efflux requires ABCA1. The presence of anti-Aβ antibodies in culture medium did not affect cholesterol efflux from cells (Fig. 3D), suggesting that ABCA1-Aβ interaction does not occur between the cell surface and the extracellular space, where antibodies to Aβ can interfere with the interaction (see, for example, Tsujita et al., 2005), but does occur within the plasma membrane or intracellular compartments.

Aβ Accelerates Cholesterol Transport From the Brain to the peripheral tissues

It is known that Aβ is transported from the brain into the circulation by receptor-mediated transcytosis across the blood–brain barrier (BBB; Shibata et al., 2000) and the choroids plexus (Crossgrove et al., 2005). This mechanism is presumed to function to clear toxic Aβ from the brain. However, we speculate that Aβ is exported from the brain to discharge cerebral cholesterol. To test this hypothesis, we examined whether intracranial cholesterol can be transported into the

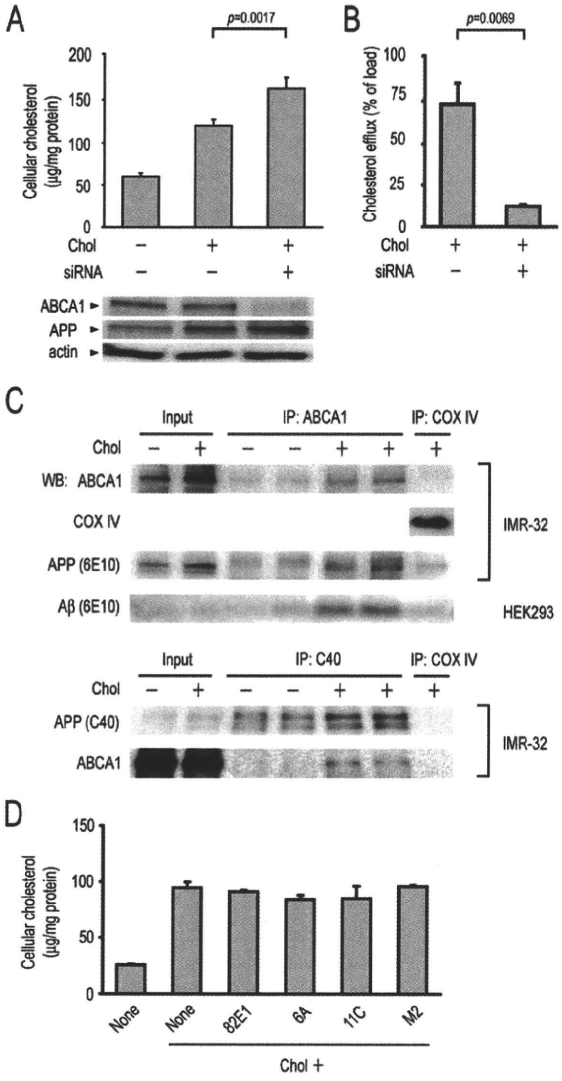

Fig. 3. Aβ-induced cholesterol efflux is mediated by ABCA1. Knocking down ABCA1 by siRNA increased cellular cholesterol levels (**A**) and decreased cholesterol efflux (**B**) in IMR-32 cells. **C:** ABCA1 and APP were immunoprecipitaed from cell lysates of non-transfected IMR-32 and APP_{SW}-transfected HEK293 cells with or without cholesterol loading and stained with antibodies to these proteins. Antibodies C40 and 6E10 recognize the C-terminal and Aβ regions of APP, respectively. A cholesterol-promoted interaction between ABCA1 and APP/Aβ was demonstrated. As a negative control, an antibody to COX-IV, a mitochondrial membrane protein, was used. **D:** IMR-32 cells were cholesterol loaded in the presence of an antibody to the N-terminus (82E1) or C-terminus (6A for Aβ40 and 11C for Aβ42) of Aβ or an antibody to FLAG (M2). None of the antibodies affected cellular cholesterol levels, suggesting that ABCA1-Aβ interaction does not occur between the cell surface and the extracellular space. All columns and bars represent the mean ± SEM (n = 3).

peripheral tissues and, if so, whether Aβ has any effect on such efflux. For this purpose, we reconstituted lipoproteins with or without Aβ using ^{14}C-cholesterols (Fig. 4A) and injected them into the cerebral ventricle of APP knockout mice. Ten or sixty minutes after injection, mice were sacrificed and dissected into tissues including the brain, heart, kidney, liver, lung, and spleen. The distribution of the injected ^{14}C-cholesterol in tissues was determined by measurement of the radioactivity of tissue homogenates. The injected cholesterol was found to be excreted rapidly from the brain into the peripheral tissues (Fig. 4B). Compared with control lipoproteins without Aβ, lipoproteins with Aβ exhibited accelerated transport from the brain to the liver (Fig. 4C). This finding supports our hypothesis that Aβ plays a role in maintenance of cerebral cholesterol homeostasis as well as of cellular cholesterol homeostasis. Even in the absence of Aβ, however, a certain amount of the injected cholesterol was excreted into the peripheral tissues. This might have occurred as a result of the function of endogenous brain apolipoproteins, such as apoE, or as a result of the conversion of cholesterol to membrane-diffusible oxysterols (Björkhem, 2006), which may have proceeded during preparation of lipoprotein-like particles.

DISCUSSION

High levels of plasma cholesterol are known to be a risk factor for AD (Solomon and Kivipelto, 2009; Stefani and Liguri, 2009). This epidemiological linkage could be explained by experimental evidence that cellular cholesterol influences the activities of both β- and γ-secretases and thereby affects Aβ production and amyloid pathology in the brain (Simons et al., 1998; Frears et al., 1999; Refolo et al., 2000; Petanceska et al., 2002; Shie et al., 2002; Grimm et al., 2008; Xiong et al., 2008). Nevertheless, it remains unclear why high levels of cholesterol increase Aβ production and what the physiological function of Aβ is.

With regard to the biochemical and physiological aspects of Aβ, there are several features common to Aβ and apoE. First, both proteins are amphiphilic and exist on HDL-like lipoproteins in the CSF (Koudinov et al., 1996). Second, each can function as a ligand for LDL receptor-related protein 1 (LRP1) and the VLDL receptor and is transported from the brain to the circulation across the BBB (Deane et al., 2008). Third, both are up-regulated in response to high cholesterol stimulation in vivo (Wu et al., 2003; Petanceska et al., 2003). These findings imply that Aβ may play a role in cholesterol transport and metabolism as a member of the apolipoproteins or in cooperation with them. In the present study, we showed that Aβ promoted efflux of cellular cholesterol during its secretion, which was mediated by ABCA1 and was accompanied by or with formation of lipoprotein-like particles. This mechanism resembles that of apolipoprotein-mediated cholesterol efflux, although apolipoproteins interact with ABCA1 from the

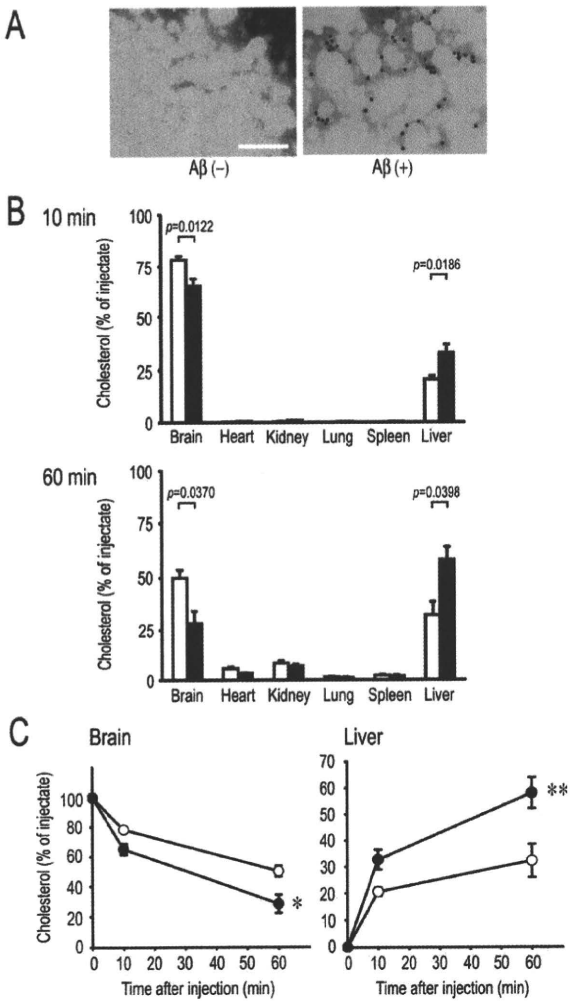

Fig. 4. Aβ accelerates cholesterol transport from the brain into the peripheral tissues. **A:** ^{14}C-labeled lipoprotein-like particles with or without Aβ were prepared. Aβ was probed with 10-nm gold particles. **B:** The reconstituted lipoproteins were injected into the cerebral ventricle of APP knockout mice (100,000 dpm/1 μl/head). At 10 and 60 min after injection, radioactivity in various tissues was measured. Approximately 60,000 dpm was successfully injected into the brain. Open columns, Aβ (–); solid columns, Aβ (+). Comparison between Aβ (+) and Aβ (–) in each tissue was performed using the unpaired Student's *t*-test. Columns and bars represent the mean ± SEM (10 min, n = 5; 60 min, n = 3). **C:** Aβ-containing lipoproteins exhibited accelerated excretion from the brain into the peripheral tissues compared with control lipoproteins. Values at each point were calculated assuming that total count of tissues represents 100% successful injection and that the counts in the brain and liver at 0 min account for 100% and 0% of the injectate, respectively. Open circles, Aβ (–); solid circles, Aβ (+). $*P = 0.0007$, $**P = 0.0011$ vs. Aβ (–), when values were compared 10–60 min after injection using two-way factorial ANOVA followed by Fisher's PLSD test. Scale bar = 100 nm.

extracellular space (Yokoyama, 2005), whereas the Aβ–ABCA1 interaction appeared to occur within the plasma membrane or intracellular compartments. Our findings suggest a novel, apolipoprotein-like function of Aβ by which Aβ participates in cellular cholesterol homeostasis. This is evidence for the biological significance of Aβ production.

A different mechanism by which Aβ regulates cellular cholesterol levels has been proposed. Grimm et al. (2005) have demonstrated that Aβ40 reduces cholesterol synthesis by inhibiting HMG-CoA reductase, whereas Aβ42 down-regulates sphingomyelin levels by activating sphingomyelinases. This finding is somewhat contrary to our finding that Aβ42 appeared to be more effective than Aβ40 in reduction of cellular cholesterol levels. Although the lower levels of cellular cholesterol we observed in APP-expressing cells likely reflect enhanced cholesterol efflux from cells rather than reduced cholesterol synthesis within cells, our results do not exclude the latter possibility. It may be that Aβ regulates cellular cholesterol levels by dual mechanisms, i.e., enhanced efflux by Aβ42 and reduced synthesis by Aβ40, both of which function as a negative feedback system against high levels of cellular cholesterol. On the other hand, Liu et al. (2007) have suggested that AICD, but not Aβ, regulates cellular and cerebral cholesterol levels through LRP1. AICD suppressed expression of the major apoE/lipoprotein receptor LRP1 and thereby reduced cellular uptake of apoE/lipoprotein. According to their hypothesis, the reduced cellular uptake of apoE/lipoprotein results in a decrease in their catabolism, which ends in increased apoE levels and decreased cholesterol levels in cells and in the brain. Consequently, cholesterol-enhanced γ-cleavage of APP, which generates not only AICD but also Aβ as a byproduct, would lead to down-regulation of cellular cholesterol levels. Our results indicate that AICD did not contribute to reduction of cellular cholesterol levels in transfected cells. However, in our assay, cholesterol was loaded onto cells not via LRP1 but by using MβCD. Thus, it is possible to assume that Aβ regulates cellular cholesterol by promoting its efflux and simultaneously AICD does so by inhibiting cellular cholesterol uptake. The lower and higher levels of cellular cholesterol that we observed in APP transgenic and knockout mouse brains may be, in part, attributable to the action of AICD. As an alternative mechanism, it is possible that Aβ or AICD induces expression of apoE, which in turn mediates cholesterol efflux from cells by interacting with ABCA1. This possibility remains to be addressed.

We also showed in the present study that Aβ accelerated transport of brain cholesterol to the peripheral tissues, at which cholesterol was injected into mouse cerebral ventricle as lipoprotein-like particles. Aβ has been demonstrated to be excreted from the brain to the circulation by receptor-mediated transcytosis at the BBB (Shibata et al., 2000) and the choroid plexus (i.e., the blood–CSF barrier; Crossgrove et al., 2005). LRP1 is the major receptor involved in this transport (Zlokovic,

2004; Johanson et al., 2008). This receptor also mediates the clearance of brain apoE to the circulation (Deane et al., 2008). Our finding implies an additional physiological function of Aβ by which Aβ transports brain cholesterol to the BBB and/or the blood–CSF barrier and discharges it into the circulation probably by a receptor-mediated mechanism. It is believed that cerebral cholesterol is excreted to the circulation at the BBB only after its conversion into 24S-hydroxycholesterol, which can cross the cell membranes more easily than cholesterol itself (Björkhem, 2006). The efflux of 24S-hydroxycholesterol to the circulation is presumed to occur by diffusion as a result of its concentration gradient between the brain and the circulation. Inversely, another oxysterol, 27-hydroxycholesterol, has been observed to be taken up by the brain from the circulation (Björkhem, 2006). This influx is also presumed to occur by diffusion dependent on its concentration gradient between the two compartments. Thus, cerebral cholesterol levels are thought to be regulated by de novo synthesis and by flux of these oxysterols and not by transport of cholesterol itself or lipoproteins. However, not a few reports have demonstrated that transcytosis of lipoproteins potentially occurs at the BBB (Dehouck et al., 1997; Balazs et al., 2004; Candela et al., 2008; Rohrer et al., 2009). In addition, 24S-hydroxycholestrol, as well as cholesterol, is not present free in plasma but is associated with acceptor proteins such as LDL and HDL (Babiker and Diczfalusy, 1998). Thus, it is likely that cerebral cholesterols including 24S-hydroxycholesterol are transported by apoE- and/or Aβ-containing lipoproteins to the BBB and/or the blood–CSF barrier and then are excreted to the circulation by transcytosis or by diffusion after dissociation from lipoproteins. Cerebral Aβ levels are regulated by de novo synthesis and degradation and also by influx and efflux at the BBB and the blood–CSF barrier (Zlokovic et al., 2000). Whereas the efflux is mediated mainly by LRP1, the influx is done primarily by the receptor for advanced glycation end products (RAGE; Zlokovic, 2004; Johanson et al., 2008). As well as the influx of oxysterols, the RAGE-mediated Aβ influx may also contribute to the regulation of cerebral cholesterol homeostasis.

The hypothesis presented here not only explains why cholesterol is a risk factor for AD but also provides new insights into the known link between apoE genotypes and AD (Corder et al., 1993). It is shown that the ability of apoE4 to mediate cholesterol efflux from cells is less than the abilities of apoE2 and apoE3 and that the presence of apoE4 therefore results in higher levels of cellular cholesterol in vitro (Michikawa et al., 2000). In addition, clearing of apoE4 from mouse brain across the BBB is less efficient than for apoE2, apoE3, and Aβ (Deane et al., 2008). Thus, the presence of apoE4 would result in enhanced Aβ production (Ye et al., 2005) to compensate for its lower cholesterol efflux, which might lead to increased accumulation of Aβ in the brain. Furthermore, compared with apoE2 and apoE3, apoE4 in the circulation is shown to be significantly taken up by cerebral microvessels and choroids plexus when allowed to form a complex with Aβ, which resulted in a moderate, but significant, transport of this complex into the brain (Martel et al., 1997). This may also contribute to enhanced amyloid pathology in patients with apoE4. Our findings also highlight a potential adverse effect of agents administered to reduce Aβ production, such as β- and γ-secretase inhibitors: inhibition of Aβ production may disturb its function in cholesterol homeostasis proposed in this study. Therefore, careful management of cholesterol may be required upon such treatments.

ACKNOWLEDGMENTS

We thank Hideki Nakagawa and Hiroo Nakagawa for their technical assistance.

REFERENCES

Babiker A, Diczfalusy U. 1998. Transport of side-chain oxidized oxysterols in the human circulation. Biochim Biophys Acta 1392:333–339.

Balazs Z, Panzenboeck U, Hammer A, Sovic A, Quehenberger O, Malle E, Sattler W. 2004. Uptake and transport of high-density lipoprotein (HDL) and HDL-associated α-tocopherol by an in vitro blood–brain barrier model. J Neurochem 89:939–950.

Björkhem I. 2006. Crossing the barrier: oxysterols as cholesterol transporters and metabolic modulators in the brain. J Intern Med 260:493–508.

Candela P, Gosselet F, Miller F, Buee-Scherrer V, Torpier G, Cecchelli R, Fenart L. 2008. Physiological pathway for low-density lipoproteins across the blood–brain barrier: transcytosis through brain capillary endothelial cells in vitro. Endothelium 15:254–264.

Corder EH, Saunders AM, Strittmatter WJ, Schmechel DE, Gaskell PC, Small GW, Roses AD, Haines JL, Pericak-Vance MA. 1993. Gene dose of apolipoprotein E type 4 allele and the risk of Alzheimer's disease in late onset families. Science 261:921–923.

Crossgrove JS, Li GJ, Zheng W. 2005. The choroid plexus removes β-amyloid from brain cerebrospinal fluid. Exp Biol Med 230:771–776.

Deane R, Sagare A, Hamm K, Parisi M, Lane S, Finn MB, Holtzman DM, Zlokovic BV. 2008. ApoE isoform-specific disruption of amyloid β peptide clearance from mouse brain. J Clin Invest 118:4002–4013.

Dehouck B, Fenart L, Dehouck MP, Pierce A, Torpier G, Cecchelli R. 1997. A new function for the LDL receptor: transcytosis of LDL across the blood–brain barrier. J Cell Biol 138:877–889.

Frears ER, Stephens DJ, Walters CE, Davies H, Austen BM. 1999. The role of cholesterol in the biosynthesis of β-amyloid. Neuroreport 10:1699–1705.

Grimm MOW, Grimm HS, Pätzold AJ, Zinser EG, Halonen R, Duering M, Tschäpe JA, De Strooper B, Müller U, Shen J, Hartmann T. 2005. Regulation of cholesterol and sphingomyelin metabolism by amyloid-β and presenilin. Nat Cell Biol 7:1118–1123.

Grimm MOW, Grimm HS, Tomic I, Beyreuther K, Hartmann T, Bergmann C. 2008. Independent inhibition of Alzheimer disease β- and γ-secretase cleavage by lowered cholesterol levels. J Biol Chem 283:11302–11311.

Hatch FT. 1968. Practical methods for plasma lipoprotein analysis. Adv Lipid Res 6:1–68.

Hsiao K, Chapman P, Nilsen S, Eckman C, Harigaya Y, Younkin S, Yang F, Cole G. 1996. Correlative memory deficits, Aβ elevation, and amyloid plaques in transgenic mice. Science 274:99–102.

Johanson CE, Duncan JA 3rd, Klinge PM, Brinker T, Stopa EG, Silverberg GD. 2008. Multiplicity of cerebrospinal fluid functions: new challenges in health and disease. Cerebrospinal Fluid Res 5:10.

Klein U, Gimpl G, Fahrenholz F. 1995. Alteration of the myometrial plasma membrane cholesterol content with b-cyclodextrin modulates

the binding affinity of the oxytocin receptor. Biochemistry 34:13784–13793.

Kontush A. 2004. Apolipoprotein Aβ: black sheep in a good family. Brain Pathol 14:433–447.

Koudinov AR, Koudinova NV, Kumar A, Beavis RC, Ghiso J. 1996. Biochemical characterization of Alzheimer's soluble amyloid β protein in human cerebrospinal fluid: association with high density lipoproteins. Biochem Biophys Res Commun 223:592–597.

Lippa CF, Ozawa K, Mann DM, Ishii K, Smith TW, Arawaka S, Mori H. 1999. Deposition of β-amyloid subtypes 40 and 42 differentiates dementia with Lewy bodies from Alzheimer disease. Arch Neurol 56:1111–1118.

Liu Q, Zerbinatti CV, Zhang J, Hoe HS, Wang B, Cole SL, Herz J, Muglia L, Bu G. 2007. Amyloid precursor protein regulates brain apolipoprotein E and cholesterol metabolism through lipoprotein receptor LRP1. Neuron 56:66–78.

Martel CL, Mackic JB, Matsubara E, Governale S, Miguel C, Miao W, McComb JG, Frangione B, Ghiso J, Zlokovic BV. 1997. Isoform-specific effects of apolipoproteins E2, E3, and E4 on cerebral capillary sequestration and blood–brain barrier transport of circulating Alzheimer's amyloid β. J Neurochem 69:1995–2004.

Matsuyama S, Teraoka R, Mori H, Tomiyama T. 2007. Inverse correlation between amyloid precursor protein and synaptic plasticity in transgenic mice. Neuroreport 18:1083–1087.

Michikawa M, Fan QW, Isobe I, Yanagisawa K. 2000. Apolipoprotein E exhibits isoform-specific promotion of lipid efflux from astrocytes and neurons in culture. J Neurochem 74:1008–1016.

Michikawa M, Gong JS, Fan QW, Sawamura N, Yanagisawa K. 2001. A novel action of Alzheimer's amyloid β-protein (Aβ): oligomeric Aβ promotes lipid release. J Neurosci 21:7226–7235.

Nishitsuji K, Tomiyama T, Ishibashi K, Ito K, Teraoka R, Lambert MP, Klein WL, Mori H. 2009. The E693Δ mutation in amyloid precursor protein increases intracellular accumulation of amyloid β oligomers and causes endoplasmic reticulum stress-induced apoptosis in cultured cells. Am J Pathol 174:957–969.

Petanceska SS, DeRosa S, Olm V, Diaz N, Sharma A, Thomas-Bryant T, Duff K, Pappolla M, Refolo LM. 2002. Statin therapy for Alzheimer's disease: will it work? J Mol Neurosci 19:155–161.

Petanceska SS, DeRosa S, Sharma A, Diaz N, Duff K, Tint SG, Refolo LM, Pappolla M. 2003. Changes in apolipoprotein E expression in response to dietary and pharmacological modulation of cholesterol. J Mol Neurosci 20:395–406.

Refolo LM, Malester B, LaFrancois J, Bryant-Thomas T, Wang R, Tint GS, Sambamurti K, Duff K, Pappolla MA. 2000. Hypercholesterolemia accelerates the Alzheimer's amyloid pathology in a transgenic mouse model. Neurobiol Dis 7:321–331.

Rohrer L, Ohnsorg PM, Lehner M, Landolt F, Rinninger F, von Eckardstein A. 2009. High-density lipoprotein transport through aortic endothelial cells involves scavenger receptor BI and ATP-binding cassette transporter G1. Circ Res 104:1142–1150.

Shibata M, Yamada S, Kumar SR, Calero M, Bading J, Frangione B, Holtzman DM, Miller CA, Strickland DK, Ghiso J, Zlokovic BV. 2000. Clearance of Alzheimer's amyloid-β_{1-40} peptide from brain by LDL receptor-related protein-1 at the blood–brain barrier. J Clin Invest 106:1489–1499.

Shie FS, Jin LW, Cook DG, Leverenz JB, LeBoeuf RC. 2002. Diet-induced hypercholesterolemia enhances brain Aβ accumulation in transgenic mice. Neuroreport 13:455–459.

Simons M, Keller P, De Strooper B, Beyreuther K, Dotti CG, Simons K. 1998. Cholesterol depletion inhibits the generation of β-amyloid in hippocampal neurons. Proc Natl Acad Sci U S A 95:6460–6464.

Solomon A, Kivipelto M. 2009. Cholesterol-modifying strategies for Alzheimer's disease. Expert Rev Neurother 9:695–709.

Stefani M, Liguri G. 2009. Cholesterol in Alzheimer's disease: unresolved questions. Curr Alzheimer Res 6:15–29.

Suga K, Tomiyama T, Mori H, Akagawa K. 2004. Syntaxin 5 interacts with presenilin holoproteins, but not with their N- or C-terminal fragments, and affects β-amyloid peptide production. Biochem J 381:619–628.

Tajima S, Yokoyama S, Yamamoto A. 1983. Effect of lipid particle size on association of apolipoproteins with lipid. J Biol Chem 258:10073–10082.

Tsujita M, Wu CA, Abe-Dohmae S, Usui S, Okazaki M, Yokoyama S. 2005. On the hepatic mechanism of HDL assembly by the ABCA1/apoA-I pathway. J Lipid Res 46:154–162.

Wu CW, Liao PC, Lin C, Kuo CJ, Chen ST, Chen HI, Kuo YM. 2003. Brain region-dependent increases in β-amyloid and apolipoprotein E levels in hypercholesterolemic rabbits. J Neural Transm 110:641–649.

Xiong H, Callaghan D, Jones A, Walker DG, Lue LF, Beach TG, Sue LI, Woulfe J, Xu H, Stanimirovic DB, Zhang W. 2008. Cholesterol retention in Alzheimer's brain is responsible for high β- and γ-secretase activities and Aβ production. Neurobiol Dis 29:422–437.

Yao ZX, Papadopoulos V. 2002. Function of β-amyloid in cholesterol transport: a lead to neurotoxicity. FASEB J 16:1677–1679.

Ye S, Huang Y, Müllendorff K, Dong L, Giedt G, Meng EC, Cohen FE, Kuntz ID, Weisgraber KH, Mahley RW. 2005. Apolipoprotein (apo) E4 enhances amyloid β peptide production in cultured neuronal cells: apoE structure as a potential therapeutic target. Proc Natl Acad Sci U S A 102:18700–18705.

Yokoyama S. 2005. Assembly of high density lipoprotein by the ABCA1/apolipoprotein pathway. Curr Opin Lipidol 16:269–279.

Zheng H, Jiang M, Trumbauer ME, Sirinathsinghji DJ, Hopkins R, Smith DW, Heavens RP, Dawson GR, Boyce S, Conner MW, Stevens KA, Slunt HH, Sisoda SS, Chen HY, Van der Ploeg LH. 1995. β-Amyloid precursor protein-deficient mice show reactive gliosis and decreased locomotor activity. Cell 81:525–531.

Zlokovic BV. 2004. Clearing amyloid through the blood–brain barrier. J Neurochem 89:807–811.

Zlokovic BV, Yamada S, Holtzman D, Ghiso J, Frangione B. 2000. Clearance of amyloid β-peptide from brain: transport or metabolism? Nat Med 6:718.

SAGE-Hindawi Access to Research
International Journal of Alzheimer's Disease
Volume 2011, Article ID 431320, 8 pages
doi:10.4061/2011/431320

Research Article

E22Δ Mutation in Amyloid β-Protein Promotes β-Sheet Transformation, Radical Production, and Synaptotoxicity, But Not Neurotoxicity

Takayuki Suzuki,[1] Kazuma Murakami,[1] Naotaka Izuo,[2] Toshiaki Kume,[2] Akinori Akaike,[2] Tetsu Nagata,[3] Tomoyuki Nishizaki,[3] Takami Tomiyama,[4] Hiroshi Takuma,[4] Hiroshi Mori,[4] and Kazuhiro Irie[1]

[1] *Laboratory of Organic Chemistry in Life Science, Division of Food Science and Biotechnology, Graduate School of Agriculture, Kyoto University, Sakyo-ku, Kyoto 606-8502, Japan*
[2] *Department of Pharmacology, Graduate School of Pharmaceutical Sciences, Kyoto University, Sakyo-ku, Kyoto 606-8501, Japan*
[3] *Department of Physiology, Hyogo College of Medicine, Nishinomiya 663-8501, Japan*
[4] *Department of Neuroscience, Graduate School of Medicine, Osaka City University, Osaka 545-8585, Japan*

Correspondence should be addressed to Kazuhiro Irie, irie@kais.kyoto-u.ac.jp

Received 16 October 2010; Accepted 16 November 2010

Academic Editor: Katsuhiko Yanagisawa

Oligomers of 40- or 42-mer amyloid β-protein (Aβ40, Aβ42) cause cognitive decline and synaptic dysfunction in Alzheimer's disease. We proposed the importance of a turn at Glu22 and Asp23 of Aβ42 to induce its neurotoxicity through the formation of radicals. Recently, a novel deletion mutant at Glu22 (E22Δ) of Aβ42 was reported to accelerate oligomerization and synaptotoxicity. To investigate this mechanism, the effects of the E22Δ mutation in Aβ42 and Aβ40 on the transformation of β-sheets, radical production, and neurotoxicity were examined. Both mutants promoted β-sheet transformation and the formation of radicals, while their neurotoxicity was negative. In contrast, E22P-Aβ42 with a turn at Glu22 and Asp23 exhibited potent neurotoxicity along with the ability to form radicals and potent synaptotoxicity. These data suggest that conformational change in E22Δ-Aβ is similar to that in E22P-Aβ42 but not the same, since E22Δ-Aβ42 exhibited no cytotoxicity, unlike E22P-Aβ42 and wild-type Aβ42.

1. Introduction

Alzheimer's disease (AD) is characterized by amyloid deposition in senile plaques that are mainly composed of 40- and 42-mer amyloid β-proteins (Aβ40 and Aβ42) [1, 2]. These proteins are secreted from amyloid precursor protein (APP) by two proteases, β- and γ-secretases [3]. Aβ42 plays a more critical role in the pathogenesis of AD than Aβ40 because of its stronger aggregative ability and neurotoxicity [3]. Oxidative stress is believed to contribute to neuronal loss in AD [4–6]; one of the proposed mechanisms of Aβ42-induced neurotoxicity is related to the radicalization at both Tyr10 and Met35 accompanied by the generation of hydrogen peroxide [7, 8]. On the other hand, soluble oligomeric assembly of Aβ causes cognitive impairment and synaptic dysfunction in AD [9, 10].

Our previous investigation using solid-state NMR together with systematic proline replacement proposed a toxic conformer with a turn at positions 22 and 23 in Aβ42 aggregates and a nontoxic conformer with a turn at positions 25 and 26; the former showed a potent ability to aggregate, form oligomers, and exhibit neurotoxicity [11]. The turn formation at positions 22 and 23 along with the neighboring β-sheet structure in the toxic conformer of Aβ42 brought Tyr10 and Met35 close together to generate the *S*-oxidized radical cation at Met35, the ultimate toxic radical species, through oxidation by the phenoxy radical at Tyr10 produced by redox reactions [7, 12]. The mutations of Aβ are concentrated at

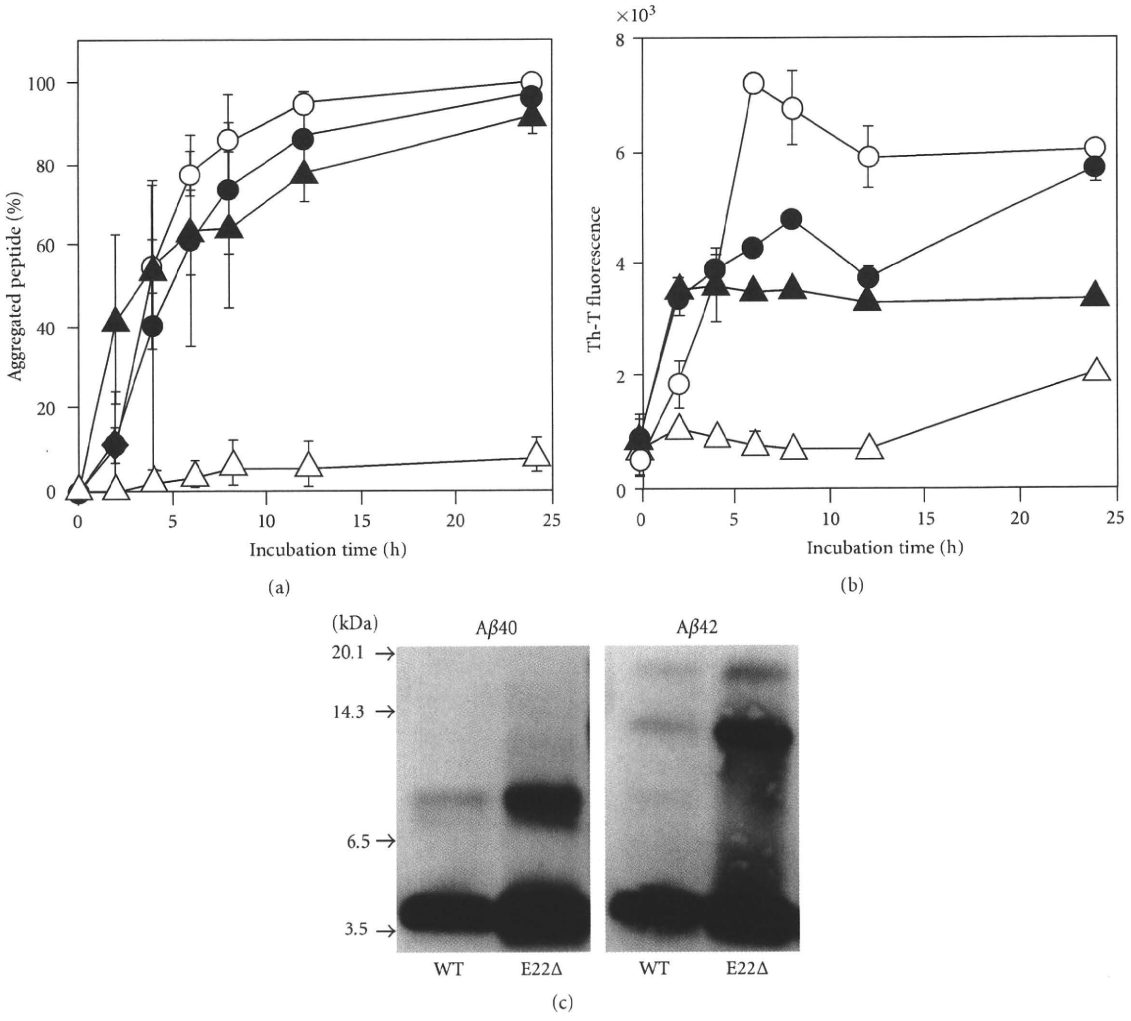

FIGURE 1: Aggregation profiles of E22Δ-Aβ40 and E22Δ-Aβ42 (25 μM) after incubation at 37°C. (a) Sedimentation assay estimated by HPLC analysis after centrifugation. (b) Th-T fluorescence assay. ○, Aβ42; △, Aβ40; ●, E22Δ-Aβ42; ▲, E22Δ-Aβ40. (c) Western blotting without incubation.

positions 21, 22, and 23; A21G (Flemish), E22G (Arctic), E22Q (Dutch), E22K (Italian), and D23N (Iowa) types. These mutations may play a pathological role in cerebral amyloid angiopathy (CAA) or familial AD (FAD) because these mutant proteins induced neuronal death *in vitro* more potently than wild-type Aβ42 [13]. Thus, Glu22 and Asp23 in Aβ are considered to be key residues for neurotoxicity through the formation of radicals.

Recently, Mori and coworkers reported that a novel mutation, in which the Glu-22 residue is defective (E22Δ), induced AD-type dementia without amyloid deposition, and that *in vitro* E22Δ-Aβ42 favorably formed low-molecular weight oligomers to inhibit long-term potentiation (LTP) compared with Aβ42 [14] and to induce synaptic alteration [15]. Therefore, the effects of the deletion at Glu22 on the secondary structure, formation of radicals, and neurotoxicity are interesting from the standpoint of discussing the role of the Glu-22 residue of Aβ42 in the pathogenesis of AD.

This paper describes a comprehensive study of the aggregative ability, secondary structure, radical-generating activity, neurotoxicity in primary rat cortical neuronal cell cultures, and the inhibitory activity of LTP of both E22Δ-Aβ40 and E22Δ-Aβ42. These results were compared with those of E22P-Aβ42 with a turn at positions 22 and 23.

2. Materials and Methods

2.1. Preparation of E22Δ-Aβ. E22Δ-Aβ40 and E22Δ-Aβ42 were synthesized by the method reported previously [16]. Their molecular weights were confirmed by matrix-assisted laser desorption/ionization time-of-flight mass spectrometry (MALDI-TOF-MS): E22Δ-Aβ40 (*m/z*: calcd: 4201.76; found:

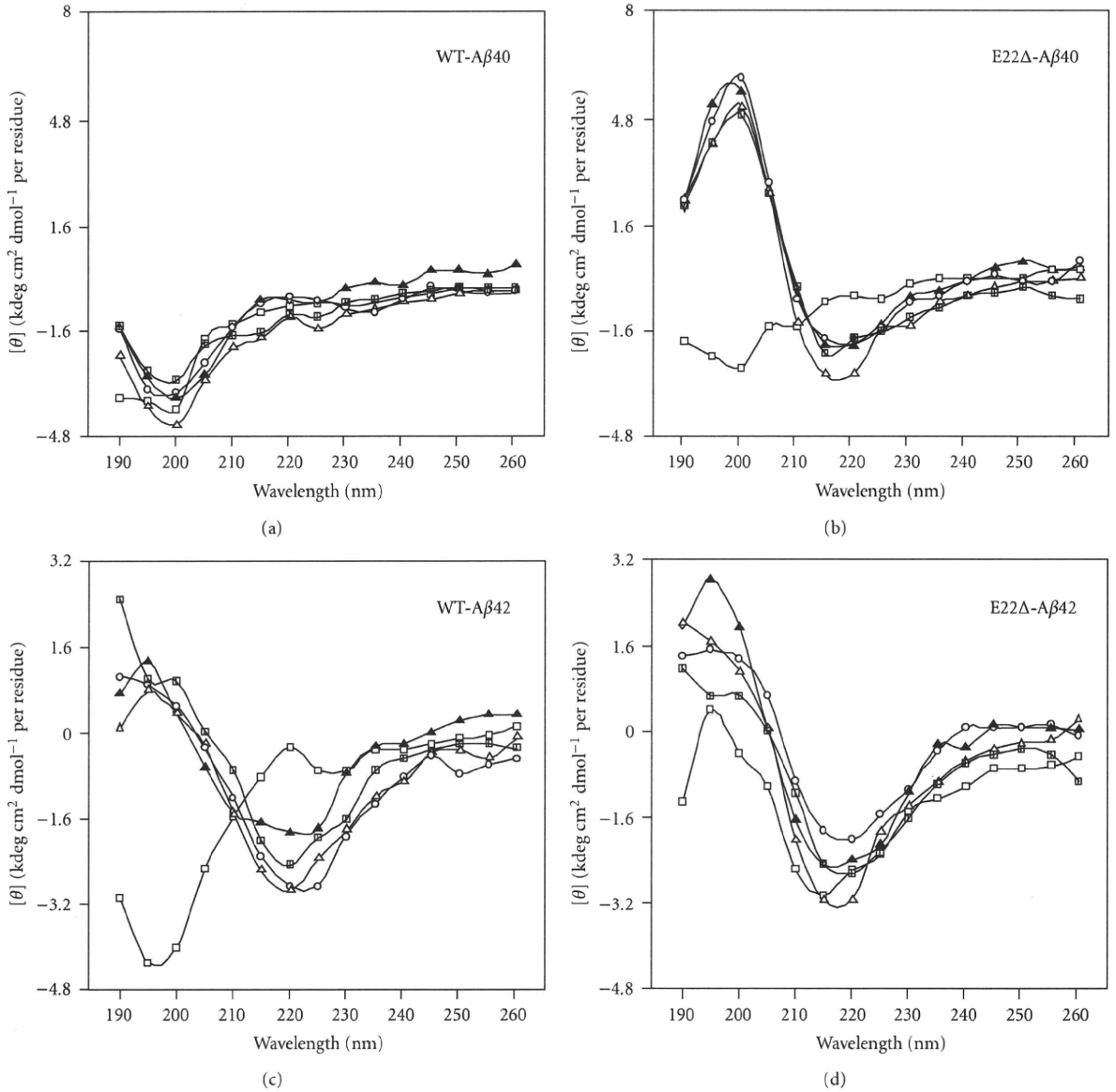

FIGURE 2: CD spectra of E22Δ-Aβ40 and E22Δ-Aβ42 (25 μM). (a) Aβ40, (b) E22Δ-Aβ40, (c) Aβ42, (d) E22Δ-Aβ42. Each Aβ (25 μM) was incubated in phosphate buffer at 37°C for the following times: □, 0 h; ▲, 4 h; △, 8 h; ∘, 24 h; ■, 48 h.

4201.56 $[M + H]^+$), E22Δ-Aβ42 (*m/z*: calcd: 4386.00; found: 4385.98 $[M + H]^+$).

2.2. Sedimentation Assay. The aggregation kinetics of each Aβ (25 μM) was estimated with the sedimentation assay using HPLC. The experimental procedure was described elsewhere [13]. The area of absorption at 220 nm was integrated and expressed as a percentage of the control.

2.3. Thioflavin T (Th-T) Fluorescence Assay. Aggregative ability of each Aβ (25 μM) was evaluated by the Th-T method developed by Naiki and Gejyo [17]. The measurement was performed on a Multidetection Microplate Reader powerscan HT (Dainippon Sumitomo Pharma) at room temperature, as described elsewhere [13]. Fluorescence intensity was measured at 450 nm excitation and 482 nm emission.

2.4. Western Blotting. Gel electrophoresis using 10–20% Tricine gel (Invitrogen, Carlsbad, CA) and Western blots analysis were carried out according to the manufacturer's protocol. The experimental procedure was described elsewhere [12]. Briefly, each Aβ was dissolved in 0.1% NH_4OH at 250 μM. After a 10-fold dilution by 50 mM sodium phosphate containing 100 mM NaCl at pH 7.4, the resultant peptide solution (25 μM) was incubated for 0, 2, or 4 hr at

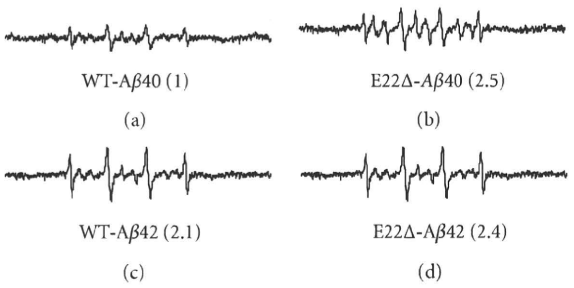

FIGURE 3: ESR spectra of E22Δ-Aβ40 and E22Δ-Aβ42 (100 μM) after 48-hr incubation at 37°C. (a) Aβ40, (b) E22Δ-Aβ40, (c) Aβ42, (d) E22Δ-Aβ42. The spectra of Aβ are shown after subtraction of the background spectrum in the presence of PBN without Aβ. Numbers in parentheses represent relative integral intensities of ESR signals, where the intensity of Aβ40 was taken as 1.0.

37°C. The anti-N-terminus of Aβ antibody, 82E1, (Immuno-Biological Laboratories Co., Ltd., Gunma, Japan) was used at 1 μg/mL as the primary antibody.

2.5. CD Spectrometry. Each Aβ was dissolved in 0.1% NH_4OH at 250 μM and diluted 10 times with 50 mM phosphate buffer (pH 7.12). The procedure was described elsewhere [16].

2.6. ESR Spectrometry. A reliable method for estimating the ability of Aβ (100 μM) to produce radicals using ESR was developed by Butterfield's group [18]. ESR spectrometry was performed on an EMX ESR spectrometer (Bruker BioSpin K.K., Karlsruhe, Germany) at room temperature, as described elsewhere [19].

2.7. Estimation of Cell Survival. To evaluate the neurotoxicity of Aβ using an MTT assay, we used undifferentiated PC12 cells, which have the potential to differentiate into neural cells, are sensitive to Aβ, and are generally used for detecting neurotoxicity as a neurotoxicity model [20]. The experimental procedure was described elsewhere [15].

2.8. Preparation of Primary Culture and Estimation of Cell Survival. Near-pure neuronal cultures were obtained from the cerebral cortices of fetal rats (17–19 days of gestation) as described [21, 22]. Cultures were maintained in Eagle's MEM supplemented with 10% heat-inactivated fetal bovine serum or 10% heat-inactivated horse serum at 37°C in a humidified 5% CO_2 atmosphere. To prevent the proliferation of nonneural cells, 10 μM cytosine β-arabinofuranoside hydrochloride was added after 5 days of plating. In all experiments mature cells used after 11–13 days *in vitro*. Animals were treated in accordance with the guidelines of the Kyoto University animal experimentation committee and the guidelines of the Japanese Pharmacological Society.

Each Aβ was dissolved in 0.02% NH_4OH at 200 μM and diluted on ice immediately before treatment. After 48 hr treatment, neurotoxicity was evaluated by lactate dehydrogenase (LDH) release assay and MTT assay.

2.9. Long-Term Potentiation. Field excitatory postsynaptic potentials (fEPSPs) were recorded from the CA1 region of rat hippocampal slices (Wistar rats, male, 6 weeks old) by electrically stimulating the Schaffer collateral [23]. Hippocampal slices were soaked in E22Δ-Aβ40, E22Δ-Aβ42, and E22P-Aβ42 solution [20 μg/200 mL phosphate-buffered saline (PBS)] before high-frequency stimulation (5 trains consisted of four 100-Hz pulses with an intertrain interval of 200 ms). fEPSPs were measured in the presence and absence of each Aβ.

3. Results and Discussion

3.1. Aggregative Ability of E22Δ Mutants. E22Δ-Aβ40 and E22Δ-Aβ42 were examined for their aggregative ability by a sedimentation assay: HPLC analysis after centrifugation of each Aβ solution. Both E22Δ-Aβ40 and E22Δ-Aβ42 aggregated at a velocity similar to Aβ42, while Aβ40 hardly aggregated even after 24-hr incubation (Figure 1(a)). This suggests that the ability to form aggregates of both E22Δ-Aβ40 and E22Δ-Aβ42 would be comparable to that of Aβ42 though soluble Aβ assemblies (oligomers) could not be distinguished from high-molecular weight fibrils in this assay condition (centrifugation: 20,000 g × 10 min). In the Th-T assay, which can estimate the β-sheet structure in Aβ aggregates [17], E22Δ-Aβ40 showed higher fluorescence than Aβ40. In contrast, the maximum fluorescence of E22Δ-Aβ42 did not exceed that of Aβ42, although the velocity of E22Δ-Aβ42 showing fluorescence was slightly higher than that of Aβ42 (Figure 1(b)). These data suggest that the E22Δ mutation accelerates the aggregation of Aβ.

Western blotting was carried out to estimate accurately the oligomerization state of Aβ. E22Δ-Aβ42 formed trimers exclusively, but E22Δ-Aβ40 produced dimers immediately after incubation (Figure 1(c)), as did the cases in the paper by Tomiyama et al. [14]; however, our Th-T assay results do not coincide with their results [14]; under Tomiyama's conditions, both mutants showed almost no fluorescence, even after 7 days. This discrepancy of the Th-T test may be due to the different conditions to make aggregates, presumably resulting in the generation of oligomers containing a β-sheet structure, as Ishii and coworkers suggested [24, 25].

3.2. Secondary Structure of E22Δ Mutants. To investigate the secondary structure of E22Δ-Aβ40 and E22Δ-Aβ42, their CD spectra were measured. In the control experiment using Aβ42 (Figure 2(c)), the positive peak at 200 nm and the negative peak at 220 nm gradually increased during the 48-hr incubation, suggesting that transformation of the random organization into a β-sheet structure occurred, while Aβ40 remained mainly random (Figure 2(a)). In contrast, E22Δ-Aβ42 formed a β-sheet-rich structure immediately after dissolution (Figure 2(d)). The velocity of the transformation of E22Δ-Aβ40 was also higher than that of Aβ42 (Figure 2(b)).

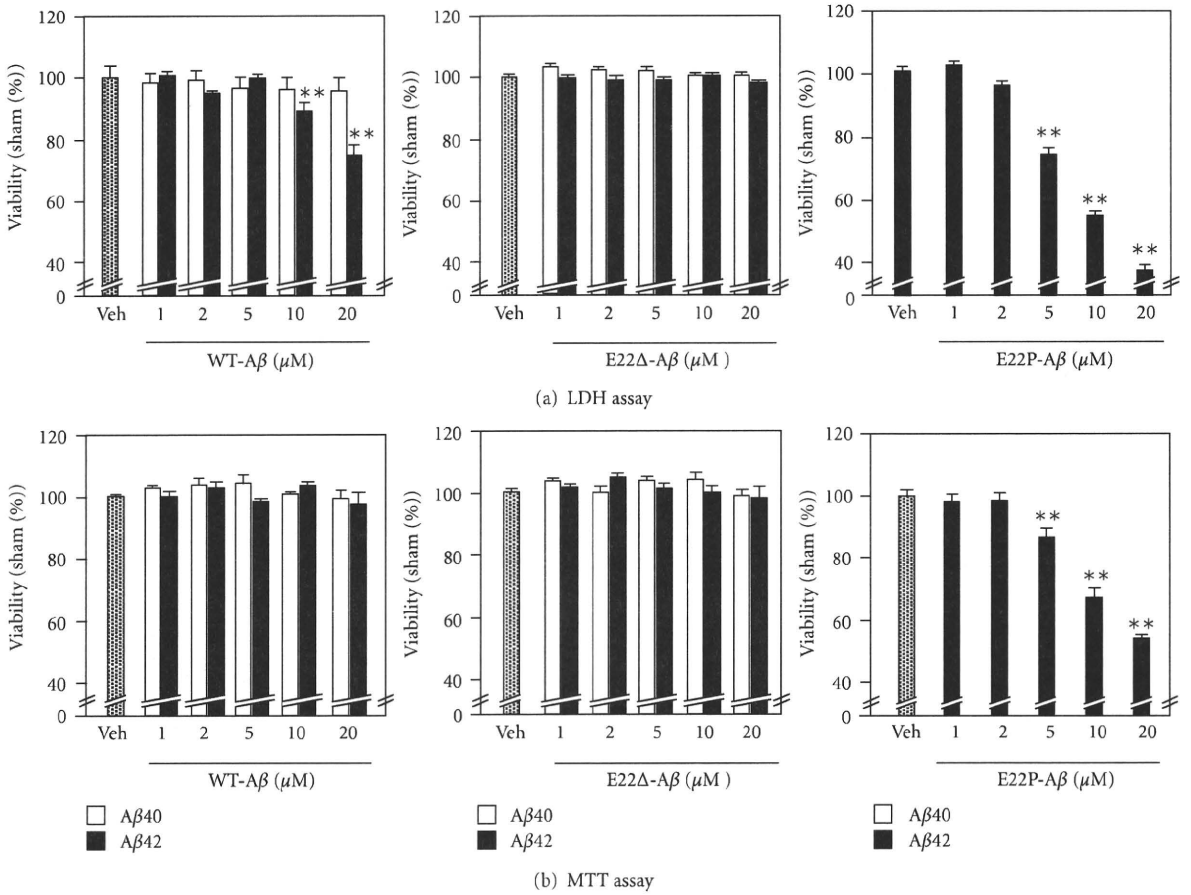

FIGURE 4: Neurotoxicity of Aβ40, Aβ42, E22Δ-Aβ40, E22Δ-Aβ42, and E22P-Aβ42 with the indicated concentration (1, 2, 5, 10, and 20 μM) using primary rat cortical neuronal cell cultures after 48-hr incubation at 37°C. Data are expressed as the mean ± s.e.m. $*P < .05$ *versus* vehicle, $**P < .01$ *versus* vehicle. Veh: vehicle.

These results suggest that the E22Δ mutation induces β-sheet transformation to form Aβ oligomers under our condition.

3.3. Radical Production by E22Δ Mutants. Our previous studies suggested that the radical productivity of Aβ42 mutants at position 22 such as E22P-, E22K-, E22Q-, and E22G-Aβ42 correlated with their aggregative ability and neurotoxicity [7]. To investigate the effect of E22Δ mutation in Aβs on the radical-generating activity, ESR was measured using phenyl-*N*-*tert*-butylnitrone (PBN) as a spin-trapping reagent (Figure 3). ESR signals of E22Δ-Aβ40 were twice more potent than those of Aβ40, and E22Δ-Aβ42 also showed slightly stronger signals than Aβ42. The radical productivity of the E22Δ-Aβs correlated basically with their ability to form oligomers and a β-sheet structure (Figures 1(c), 2).

3.4. Neurotoxicity of E22Δ-Aβs in Primary Rat Cortical Neuronal Cell Cultures. Having demonstrated that E22Δ mutation enhanced the β-sheet structure and radical productivity, we assessed the effect of this mutation on the neurotoxicity in primary rat cortical neuronal cell cultures by LDH and MTT assay (Figure 4). Treatment of the neurons with 1–20 μM of wild-type Aβ42 for 2 days induced neurotoxicity in a dose-dependent manner in the LDH test (Figure 4(a), left), in which the released LDH of the damaged cells (mainly neurons) was measured in the medium. E22P-Aβ42 with a turn at positions 22, and 23 induced stronger damage to the neurons than wild-type Aβ42; cell viability was less 40% at 20 μM (Figure 4(a), right). On the other hand, the difference in cell viability between the vehicle and wild-type Aβ42 did not reach a significant level in the MTT assay even at 20 μM (Figure 4(b), left). The cell viability of E22P-Aβ42 in MTT was also about 50% at 20 μM. In the MTT assay, total cells containing neurons, astrocytes, and microglia damaged by Aβs were counted. Since the neurons are more sensitive to damage than astrocytes or microglia in the primary cell cultures [26], the "neurotoxicity" estimated by the LDH test is often stronger than that evaluated by the MTT test.

It is worth noting that E22Δ-Aβ40 and E22Δ-Aβ42 as well as Aβ40 at 20 μM failed to show neurotoxicity against the primary cultures both in the LDH and MTT tests (Figure 4). These results are consistent with those reported by Takuma

et al.; the neurotoxicity of E22Δ-Aβ42 was very weak against mouse neuroblastoma Neuro-2a and human neuroblastoma IMR-32 [15]. In our MTT test using rat neuroblastoma PC12 cells, the IC_{50} of E22Δ-Aβ42 and wild-type Aβ42 was $4.6 \pm 1.1\,\mu M$ and $0.65 \pm 0.11\,\mu M$, respectively, showing that E22Δ-Aβ42 was significantly less toxic than wild-type Aβ42. The neurotoxicity of E22Δ-Aβ40 ($IC_{50} = 10 \pm 1.0\,\mu M$) was weak as expected, but slightly stronger than that of Aβ40 ($IC_{50} = 20 \pm 1.0\,\mu M$).

3.5. Synaptotoxicity of E22Δ Mutants. Selkoe and coworkers suggested that Aβ dimers are the smallest synaptotoxic species inhibiting the LTP in the pathogenesis of AD and that plaque cores are largely inactive but sequester and release dimers [27]. Tomiyama et al. reported the more potent inhibition of LTP by E22Δ-Aβ42 than by wild-type Aβ42 [14]. We tested the inhibition of LTP by E22Δ-Aβ40 using rat hippocampal slices. Figure 5 shows that E22Δ-Aβ40 is not such a potent inhibitor of LTP as E22Δ-Aβ42, whose inhibitory potency was stronger that of than wild-type Aβ42, as Tomiyama et al. reported [14]. This coincides with the previous datas that the 42-mer Aβ showed more potent neurotoxicity than 40-mer Aβ [13]. Notably, E22P-Aβ42, which can more readily form a toxic conformer with a turn at positions 22 and 23 than wild-type Aβ42 [11], inhibited the LTP more strongly than E22Δ-Aβ42 at an almost undetectable level after 60 min (Figure 5(b)). This suggests that the conformation at positions 22 and 23 of E22P-Aβ42 might be similar to that of E22Δ-Aβ42 at positions 21 and 23.

3.6. Relevance of E22Δ Mutation to Turn-Induced Neurotoxicity. The present results suggest that E22Δ mutation in Aβ accelerates the transformation of a random form into a β-sheet structure (Figure 2) and radical productivity (Figure 3) but does not increase neurotoxicity in primary rat cortical neuronal cell cultures (Figure 4). E22Δ-Aβ42 synthesized in our laboratory showed the significant formation of oligomers (Figure 1) and synaptotoxicity (Figure 5), as reported by Mori and coworkers [14]. In addition, E22P-Aβ42 inhibited LTP more severely than E22Δ-Aβ42 (Figure 5). We previously reported that E22P-Aβ42, with a turn at positions 22 and 23 as a Pro-X corner (X: variable amino acid residue) [28], could form significant oligomers [11] with a β-sheet-rich structure [16] and radicals to result in potent neurotoxicity with the formation of radicals [7]; therefore, E22Δ-induced synaptotoxicity might be in part related to turn-induced radical formation. This implies that conformational change in E22Δ-Aβ is similar to that in E22P-Aβ42, but is not the same since E22Δ-Aβ42 exhibited no neurotoxicity, unlike E22P-Aβ42 and wild-type Aβ42.

It should be noted that the effects of E22Δ mutation on the physicochemical properties of Aβ40 are significantly higher than those of Aβ42. This tendency is similar to cases of other CAA or FAD mutant Aβs. We previously reported a comprehensive study on the aggregation, neurotoxicity, and secondary structure of Aβ mutants at positions 21–23 (A21G, E22G, E22Q, E22K, and D23N) [13]. Since Aβ40

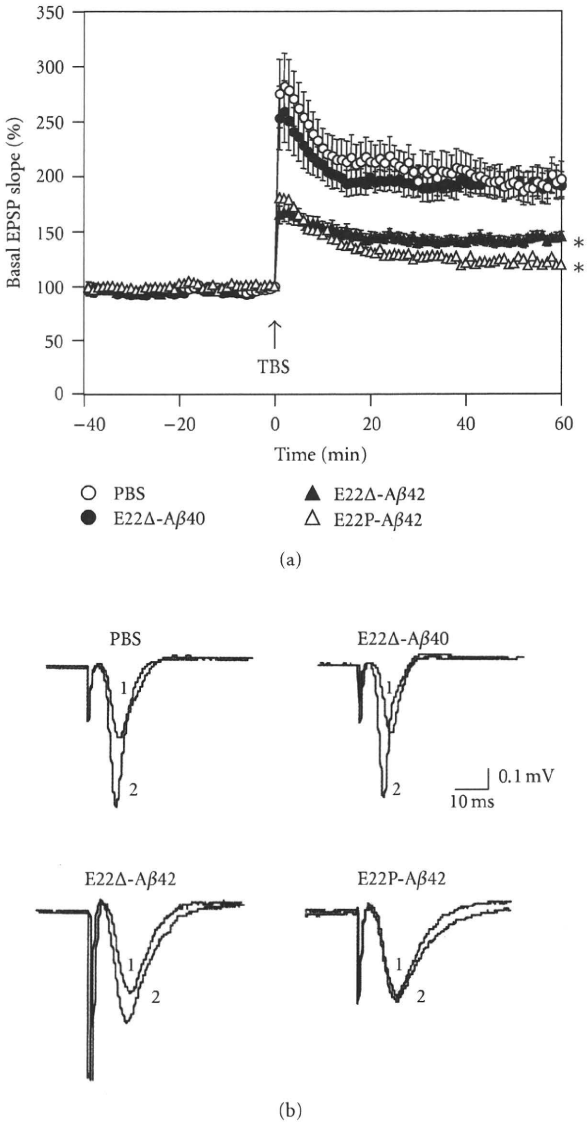

FIGURE 5: *In vivo* synaptotoxicity of E22Δ-Aβ40, E22Δ-Aβ42, and E22P-Aβ42 estimated by LTP expression. (a) Field excitatory postsynaptic potentials (fEPSPs) were recorded from the CA1 region of rat hippocampal slices (Wistar rats, male, 6 weeks old) by delivering theta burst stimulation (TBS) to the Schaffer collateral/commissural pathway. LTP was induced by high-frequency stimulation (5 trains consisted of four 100-Hz pulses with an intertrain interval of 200 ms) in the presence and absence of each Aβ (20 μg/200 mL PBS), to be injected into the lateral ventricle 20 min before stimulation. Each point on the graph represents the mean ± s.e.m. of basal fEPSP slope (0 min); $n = 12$ for PBS, $n = 9$ for E22Δ-Aβ40, $n = 10$ for E22Δ-Aβ42, and $n = 10$ for E22P-Aβ40. $^*P < .0001$ versus PBS; $P = .4258$ between PBS and E22Δ-Aβ40. $P < .0001$ versus PBS, when fEPSP slopes were compared with 1 to 60 min after TBS. The means between the four groups were compared using analysis of variance followed by Fisher's protected least significant difference (PLSD) test. ○, PBS; •, E22Δ-Aβ40; ▲, E22Δ-Aβ42; △, E22P-Aβ42. (b) Typical field excitatory postsynaptic potentials at (1) 0 and (2) 60 minutes after TBS.

is secreted in neurons about nine times more abundantly than Aβ42 [3], in some cases Aβ40 may play a critical role in the pathogenesis of CAA or FAD. In addition, the E22Δ mutant of Aβ40 [14] as well as the CAA- or FAD-related Aβ40 mutants at positions 21, 22, and 23 have been reported to be more resistant than wild-type Aβ40 against degradation by insulin-degrading enzyme [29]; however, it remains controversial whether E22Δ is a familial type of AD or AD-type dementia.

Mori, Tomiyama, and coworkers implied the intracellular accumulation of Aβ oligomers using cultured cells [30] and their own developed mouse model [31] with E22Δ mutation. This mutation also caused apoptosis induced by stress in the endoplasmic reticulum [30]. Quite recently, we proposed the involvement of a turn at positions 22 and 23 of Aβ in intracellular amyloidosis [32]. Thus, the increase of radical productivity by E22Δ mutation is in good agreement with the turn-induced oxidative stress of Aβ42 [7], presumably *via* the interplay between Tyr10 and Met35 [12]. The deletion mutation of the residue at position 22 might promote Tyr10 in close proximity to the sulfur atom of Met35, inducing the effective production of radicals.

4. Conclusion

In summary, E22Δ-Aβ42 effectively induced the transformation of a random form to a β-sheet structure and the formation of radicals accompanied with oligomerization. However, the molecular mechanism of the pathology of AD of E22Δ-Aβ42 might be different from that of wild-type Aβ42 since E22Δ-Aβ42 showed more potent synaptotoxicity but weaker neurotoxicity than wild-type Aβ42.

Acknowledgments

The authors thank Dr. Hiroyuki Fukuda at the Institute of Medical Science, The University of Tokyo for MALDI-TOF-MS measurements, and Drs. Noriaki Kinoshita and Yuko Horikoshi-Sakuraba at Immuno-Biological Laboratories Co., Ltd. for providing the antibody 82E1. This research was supported in part by grants-in-aid for Scientific Research (A) (Grant no. 21248015 to K.I.) and Scientific Research (C) (Grant no. 22603006 to K.M.) from the Ministry of Education, Culture, Sports, Science and Technology of the Japanese Government and in part by the Alzheimer's Association (IIRG-09-132098) to HM.

References

[1] G. G. Glenner and C. W. Wong, "Alzheimer's disease: initial report of the purification and characterization of a novel cerebrovascular amyloid protein," *Biochemical and Biophysical Research Communications*, vol. 120, no. 3, pp. 885–890, 1984.

[2] C. L. Masters, G. Simms, and N. A. Weinman, "Amyloid plaque core protein in Alzheimer disease and Down syndrome," *Proceedings of the National Academy of Sciences of the United States of America*, vol. 82, no. 12, pp. 4245–4249, 1985.

[3] C. Haass and D. J. Selkoe, "Soluble protein oligomers in neurodegeneration: lessons from the Alzheimer's amyloid β-peptide," *Nature Reviews Molecular Cell Biology*, vol. 8, no. 2, pp. 101–112, 2007.

[4] C. Behl, J. B. Davis, R. Lesley, and D. Schubert, "Hydrogen peroxide mediates amyloid β protein toxicity," *Cell*, vol. 77, no. 6, pp. 817–827, 1994.

[5] D. A. Butterfield, "Amyloid β-peptide [1–42]-assosiated free radical-induced oxidative stress and neurodegeneration in Alzheimer's disease brain: mechanisms and consequences," *Current Medicinal Chemistry*, vol. 10, no. 24, pp. 2651–2659, 2003.

[6] K. J. Barnham, C. L. Masters, and A. I. Bush, "Neurodegenerative diseases and oxidatives stress," *Nature Reviews Drug Discovery*, vol. 3, no. 3, pp. 205–214, 2004.

[7] K. Murakami, K. Irie, H. Ohigashi et al., "Formation and stabilization model of the 42-mer Aβ radical: implications for the long-lasting oxidative stress in Alzheimer's disease," *Journal of the American Chemical Society*, vol. 127, no. 43, pp. 15168–15174, 2005.

[8] K. Murakami, Y. Masuda, T. Shirasawa, T. Shimizu, and K. Irie, "The turn formation at positions 22 and 23 in the 42-mer amyloid β peptide: the emerging role in the pathogenesis of Alzheimer's disease," *Geriatrics and Gerontology International*, vol. 10, supplement 1, pp. S169–S179, 2010.

[9] D. M. Walsh, I. Klyubin, J. V. Fadeeva et al., "Naturally secreted oligomers of amyloid β protein potently inhibit hippocampal long-term potentiation in vivo," *Nature*, vol. 416, no. 6880, pp. 535–539, 2002.

[10] R. Roychaudhuri, M. Yang, M. M. Hoshi, and D. B. Teplow, "Amyloid β-protein assembly and Alzheimer disease," *Journal of Biological Chemistry*, vol. 284, no. 8, pp. 4749–4753, 2009.

[11] Y. Masuda, S. Uemura, R. Ohashi et al., "Identification of physiological and toxic conformations in Aβ42 aggregates," *ChemBioChem*, vol. 10, no. 2, pp. 287–295, 2009.

[12] K. Murakami, H. Hara, Y. Masuda, H. Ohigashi, and K. Irie, "Distance measurement between Tyr10 and Met35 in amyloid beta by site-directed spin-labeling ESR spectroscopy: implications for the stronger neurotoxicity of Aβ42 than Aβ40," *Chembiochem*, vol. 8, no. 18, pp. 2308–2314, 2007.

[13] K. Murakami, K. Irie, A. Morimoto et al., "Neurotoxicity and physicochemical properties of Aβ mutant peptides from cerebral amyloid angiopathy: implication for the pathogenesis of cerebral amyloid angiopathy and Alzheimer's disease," *Journal of Biological Chemistry*, vol. 278, no. 46, pp. 46179–46187, 2003.

[14] T. Tomiyama, T. Nagata, H. Shimada et al., "A new amyloid β variant favoring oligomerization in Alzheimer's-type dementia," *Annals of Neurology*, vol. 63, no. 3, pp. 377–387, 2008.

[15] H. Takuma, R. Teraoka, H. Mori, and T. Tomiyama, "Amyloid-β E22Δ variant induces synaptic alteration in mouse hippocampal slices," *NeuroReport*, vol. 19, no. 6, pp. 615–619, 2008.

[16] K. Murakami, K. Irie, A. Morimoto et al., "Synthesis, aggregation, neurotoxicity, and secondary structure of various Aβ1–42 mutants of familial Alzheimer's disease at positions 21–23," *Biochemical and Biophysical Research Communications*, vol. 294, no. 1, pp. 5–10, 2002.

[17] H. Naiki and F. Gejyo, "Kinetic analysis of amyloid fibril formation," *Methods in Enzymology*, vol. 309, pp. 305–318, 1999.

[18] S. Varadarajan, J. Kanski, M. Aksenova, C. Lauderback, and D. A. Butterfield, "Different mechanisms of oxidative stress and neurotoxicity for Alzheimer's Aβ(1–42) and Aβ(25–35)",

Journal of the American Chemical Society, vol. 123, no. 24, pp. 5625–5631, 2001.

[19] K. Murakami, M. Uno, Y. Masuda, T. Shimizu, T. Shirasawa, and K. Irie, "Isomerization and/or racemization at Asp23 of Aβ42 do not increase its aggregative ability, neurotoxicity, and radical productivity in vitro," *Biochemical and Biophysical Research Communications*, vol. 366, no. 3, pp. 745–751, 2008.

[20] M. S. Shearman, C. I. Ragan, and L. L. Iversen, "Inhibition of PC12 cell redox activity is a specific, early indicator of the mechanism of β-amyloid-mediated cell death," *Proceedings of the National Academy of Sciences of the United States of America*, vol. 91, no. 4, pp. 1470–1474, 1994.

[21] T. Kume, H. Kouchiyama, S. Kaneko et al., "BDNF prevents NO mediated glutamate cytotoxicity in cultured cortical neurons," *Brain Research*, vol. 756, no. 1-2, pp. 200–204, 1997.

[22] T. Kume, H. Nishikawa, H. Tomioka et al., "p75-mediated neuroprotection by NGF against glutamate cytotoxicity in cortical cultures," *Brain Research*, vol. 852, no. 2, pp. 279–289, 2000.

[23] T. Nishizaki, T. Nomura, T. Matuoka et al., "The anti-dementia drug nefiracetam facilitates hippocampal synaptic transmission by functionally targeting presynaptic nicotinic ACh receptors," *Molecular Brain Research*, vol. 80, no. 1, pp. 53–62, 2000.

[24] S. Chimon and Y. Ishii, "Capturing intermediate structures of Alzheimer's β-amyloid, Aβ(1–40), by solid-state NMR spectroscopy," *Journal of the American Chemical Society*, vol. 127, no. 39, pp. 13472–13473, 2005.

[25] S. Chimon, M. A. Shaibat, C. R. Jones, D. C. Calero, B. Aizezi, and Y. Ishii, "Evidence of fibril-like β-sheet structures in a neurotoxic amyloid intermediate of Alzheimer's β-amyloid," *Nature Structural and Molecular Biology*, vol. 14, no. 12, pp. 1157–1164, 2007.

[26] M. R. Vargas and J. A. Johnson, "The Nrf2-ARE cytoprotective pathway in astrocytes," *Expert reviews in molecular medicine*, vol. 11, p. e17, 2009.

[27] G. M. Shankar, S. Li, T. H. Mehta et al., "Amyloid-β protein dimers isolated directly from Alzheimer's brains impair synaptic plasticity and memory," *Nature Medicine*, vol. 14, no. 8, pp. 837–842, 2008.

[28] P. Y. Chou and G. D. Fasman, "β-Turns in proteins," *Journal of Molecular Biology*, vol. 115, no. 2, pp. 135–175, 1977.

[29] L. Morelli, R. Llovera, S. A. Gonzalez et al., "Differential degradation of amyloid β genetic variants associated with hereditary dementia or stroke by insulin-degrading enzyme," *Journal of Biological Chemistry*, vol. 278, no. 26, pp. 23221–23226, 2003.

[30] K. Nishitsuji, T. Tomiyama, K. Ishibashi et al., "The E693Δ mutation in amyloid precursor protein increases intracellular accumulation of amyloid β oligomers and causes endoplasmic reticulum stress-induced apoptosis in cultured cells," *American Journal of Pathology*, vol. 174, no. 3, pp. 957–969, 2009.

[31] T. Tomiyama, S. Matsuyama, H. Iso et al., "A mouse model of amyloid β oligomers: their contribution to synaptic alteration, abnormal tau phosphorylation, glial activation, and neuronal loss in vivo," *Journal of Neuroscience*, vol. 30, no. 14, pp. 4845–4856, 2010.

[32] K. Murakami, Y. Horikoshi-Sakuraba, N. Murata et al., "Monoclonal antibody against the turn of the 42-residue amyloid beta protein at positions 22 and 23," *ACS Chemical Neuroscience*, vol. 1, no. 11, pp. 747–756, 2010.

Neurobiology of Disease

In Vivo Positron Emission Tomographic Imaging of Glial Responses to Amyloid-β and Tau Pathologies in Mouse Models of Alzheimer's Disease and Related Disorders

Jun Maeda,[1] Ming-Rong Zhang,[1] Takashi Okauchi,[1] Bin Ji,[1] Maiko Ono,[1] Satoko Hattori,[1] Katsushi Kumata,[1] Nobuhisa Iwata,[2] Takaomi C. Saido,[2] John Q. Trojanowski,[3] Virginia M.-Y. Lee,[3] Matthias Staufenbiel,[4] Takami Tomiyama,[5] Hiroshi Mori,[5] Toshimitsu Fukumura,[1] Tetsuya Suhara,[1] and Makoto Higuchi[1]

[1]Molecular Imaging Center, National Institute of Radiological Sciences, Chiba, Chiba 263-8555, Japan, [2]Laboratory for Proteolytic Neuroscience, RIKEN Brain Science Institute, Wako, Saitama 351-0198, Japan, [3]Center for Neurodegenerative Disease Research, University of Pennsylvania, Philadelphia, Pennsylvania 19104, [4]Novartis Institutes for Biomedical Research-Basel, CH-4002 Basel, Switzerland, and [5]Department of Neuroscience, Osaka City University Graduate School of Medicine, Osaka, Osaka 545-8585, Japan

Core pathologies of Alzheimer's disease (AD) are aggregated amyloid-β peptides (Aβ) and tau, and the latter is also characteristic of diverse neurodegenerative tauopathies. These amyloid lesions provoke microglial activation, and recent neuroimaging technologies have enabled visualization of this response in living brains using radioligands for the peripheral benzodiazepine receptor also known as the 18 kDa translocator protein (TSPO). Here, we elucidated contributions of Aβ and tau deposits to *in vivo* TSPO signals in pursuit of mechanistic and diagnostic significance of TSPO imaging in AD and other tauopathies. A new antibody to human TSPO revealed induction of TSPO-positive microgliosis by tau fibrils in tauopathy brains. Emergence of TSPO signals before occurrence of brain atrophy and thioflavin-S-positive tau amyloidosis was also demonstrated in living mice transgenic for mutant tau by positron emission tomography (PET) with two classes of TSPO radioligands, [^{11}C]AC-5216 and [^{18}F]fluoroethoxy-DAA1106. Meanwhile, only modest TSPO elevation was observed in aged mice modeling Aβ plaque deposition, despite the notably enhanced *in vivo* binding of amyloid radiotracer, [^{11}C]Pittsburgh Compound-B, to plaques. In these animals, [^{11}C]AC-5216 yielded better TSPO contrasts than [^{18}F]fluoroethoxy-DAA1106, supporting the possibility of capturing early neurotoxicity with high-performance TSPO probes. Furthermore, an additional line of mice modeling intraneuronal Aβ accumulation displayed elevated TSPO signals following noticeable neuronal loss, unlike TSPO upregulation heralding massive neuronal death in tauopathy model mice. Our data corroborate the utility of TSPO-PET imaging as a biomarker for tau-triggered toxicity, and as a complement to amyloid scans for diagnostic assessment of tauopathies with and without Aβ pathologies.

Introduction

Hallmark fibrillar pathologies in Alzheimer's disease (AD) are classified into senile plaques and neurofibrillary tangles (NFTs) composed of self-polymerized amyloid-β peptide (Aβ) and tau proteins, respectively. As initiators of a cascade-like neuronal deterioration, Aβ and tau fibrils have been targeted by developments of diagnostic and therapeutic agents, and *in vivo* detection of the Aβ plaque formation in brains of AD patients and amyloid precursor protein (APP) transgenic (Tg) mice has been enabled by positron emission tomography (PET) with [^{11}C]Pittsburgh Compound-B ([^{11}C]PIB) and other amyloid-binding radiochemicals (Klunk et al., 2004; Maeda et al., 2007). Meanwhile, imaging techniques for assessing amyloid-induced neurotoxicities remain to be established. A large number of studies documented the informativeness of volumetric magnetic resonance imaging (MRI) and metabolic PET with [^{18}F]fluoro-deoxy-glucose ([^{18}F]FDG) in quantifying neuronal damages consequent to brain amyloidoses, but these assays do not necessarily reflect the degrees of ongoing neurotoxic insults.

It is well known that amyloid deposition triggers microglial and astroglial activation in AD brains (McGeer and McGeer, 1995). Moreover, beneficial outcomes of Aβ and tau immunizations in humans and mouse models have highlighted crucial roles of immunocompetent glia in the protection of neurons against amyloid toxicities (Dodel et al., 2003; Asuni et al., 2007). By contrast, our previous study of tau Tg mice demonstrated mitigation of tau-induced neurodegeneration by attenuating neuroinflam-

Received June 13, 2010; revised Feb. 4, 2011; accepted Feb. 4, 2011.

Author contributions: J.M., M.-R.Z., T.O., B.J., T. C. Saido, J.Q.T., V.M.-Y.L., M.S., T.T., H.M., T.F., T. Suhara, and M.H. designed research; J.M., M.-R.Z., T.O., B.J., M.O., S.H., K.K., N.I., T. C. Saido, T.T., H.M., T.F., T. Suhara, and M.H. performed research; J.M., B.J., M.O., S.H., K.K., N.I., and M.H. analyzed data; J.M., M.-R.Z., J.Q.T., V.M.-Y.L., M.S., T. Suhara, and M.H. wrote the paper.

This work was supported in part by grants from the National Institute on Aging of the National Institutes of Health (AG10124 and AG17586 to J.Q.T. and V.M.-Y.L., respectively) and by Grants-in-Aid for Young Scientists (B) 20790047 (J.M.), Grants-in-Aid for the Molecular Imaging Program and Scientific Research on Priority Areas, and Research on Pathomechanisms of Brain Disorders Grant 20023036 (M.H.) from the Ministry of Education, Culture, Sports, Science and Technology, Japan. We thank Taisho Pharmaceutical (Tokyo, Japan) for providing DAA1123. We also thank Takeharu Minamihisamatsu for technical assistance, staff of the Molecular Probe Group, National Institute of Radiological Sciences, for support with radiosynthesis, and Dr. Haruhisa Inoue of Kyoto University for critical discussion.

The authors declare no competing financial interests.

Correspondence should be addressed to Dr. Makoto Higuchi, Molecular Imaging Center, National Institute of Radiological Sciences, 4-9-1 Anagawa, Inage-ku, Chiba, Chiba 263-8555, Japan. E-mail: mhiguchi@nirs.go.jp.

DOI:10.1523/JNEUROSCI.3076-10.2011

 0270-6474/11/314720-11$15.00/0

mation with an immunosuppressant (Yoshiyama et al., 2007). These contradictory functions of activated glia in pathological conditions have elevated the significance of neuroimaging systems capable of monitoring toxic conversion of glia in response to amyloidogenesis, toward the aim of therapeutically regulating glial activities at a desirable level and mode.

Upregulation of 18 kDa translocator protein (TSPO), also known as peripheral benzodiazepine receptor, in activated glia is of diagnostic importance in neurological diseases (Diorio et al., 1991), and several different PET radioligands for this molecule are now available or in development. Elevated TSPO levels in living AD brains were initially detected by [^{11}C]PK11195 (Cagnin et al., 2001), and compounds with improved blood–brain barrier permeability and affinity for TSPO, including [^{11}C]DAA1106 (Maeda et al., 2004) and [^{18}F]fluoroethoxy-DAA1106 ([^{18}F]FEDAA1106) (Zhang et al., 2004), were developed and applied to neuroimaging of AD patients (Yasuno et al., 2008). Autoradiographic assays of model mice using [^{18}F]FEDAA1106 combined with immunohistochemistry have also indicated that microglial TSPO expression is linked to toxic injuries of neurons and may herald neuronal death (Yoshiyama et al., 2007; Ji et al., 2008). Furthermore, we have developed a novel class of TSPO ligands, [^{11}C]AC-5216 (Zhang et al., 2007) and its analogs (Yanamoto et al., 2009a,b), exhibiting faster kinetics in the brain than DAA1106 families. These probes potentially produce high-contrast TSPO images and are thus likely to allow assessment of neurotoxic insults from an early pathogenic stage.

The present study examined the interplay between fibrillar Aβ and tau amyloid and TSPO-expressing microglia and *in vivo* detectability of Aβ- and tau-associated microgliosis by PET imaging of APP and tau Tg mice with [^{11}C]AC-5216 and [^{18}F]FEDAA1106. TSPO-PET was also supplemented by imaging of plaques with [^{11}C]PIB and immunostaining of postmortem human and mouse brains.

Materials and Methods

Neuropathological analyses of TSPO-positive glia in postmortem human brains. Postmortem human brains were obtained from autopsies for patients with AD, Pick's disease, progressive supranuclear palsy (PSP), and nonneurological conditions at the University of Pennsylvania Center for Neurodegenerative Disease Research, as described previously (Trojanowski, 2008). Tissues were fixed in 10% neutral buffered formalin and embedded in paraffin blocks. Representative 6-μm-thick sections were stained with a newly developed rabbit polyclonal antibody (NP157) against a synthetic peptide spanning residues 157–169 of human TSPO (DNHGWRGGRRLPE). Sections were also labeled with a fluorescent amyloid dye, (E,E)-1-fluoro-2,5-bis(3-hydroxycarbonyl-4-hydroxy) styrylbenzene (FSB; Dojindo Laboratories), as described previously (Sato et al., 2004; Higuchi et al., 2005). Similarly, rabbit polyclonal antibodies against mouse TSPO (NP155) (Ji et al., 2008) and ionized calcium binding adapter molecule-1 (Iba-1; Wako Pure Chemicals), mouse monoclonal antibodies against phosphorylated tau proteins (AT8; Endogen), NeuN (clone A60; Millipore Bioscience Research Reagents/Millipore) and general (clone 6E10; Covance) and N-terminally truncated, pyroglutamylated (AβN3pE; clone 1A10; Immuno-Biological Laboratories) Aβ peptides, and rat monoclonal antibody against glial fibrillary acidic protein (GFAP) (2.2B10; Zymed/Invitrogen) were used for multicolor fluorescence microscopy.

Animals. The animals were maintained and handled in accordance with recommendations of the National Institutes of Health and institutional guidelines at the National Institute of Radiological Sciences. All animal experiments conducted here were approved by the Animal Ethics Committee of the National Institute of Radiological Sciences.

Tg mice (PS19 line) overexpressing the P301S mutant human tau under the control of mouse prion promoter (Yoshiyama et al., 2007) were created on a B6C3H/F1 background (Yoshiyama et al., 2007), and mice aged from 3 to 15 months were used for the experiments. Tg mice termed APP23, which overexpress the Swedish doubly mutant APP751 under the control of a neuron-specific Thy-1 promoter element (Sturchler-Pierrat et al., 1997), were maintained on a C57BL/6J background, and mice aged from 12 to 26 months were examined. Tg mice overexpressing human APP with the E693Δ mutation under the control of mouse prion promoter were generated on a B6C3H/F1 background, and were backcrossed with C57BL/6J mice at least 10 times (Tomiyama et al., 2010). Non-Tg (nTg) littermates were also used as wild-type controls. Tg and nTg offspring were identified by PCR assays of tail DNA.

Generation of MRI template. A 12-month-old C57BL/6J mouse was lethally anesthetized by pentobarbital. The mouse head was embedded in 3% aqueous agarose and scanned by 9.4-Tesla Bruker AVANCE 400WB imaging spectrometer (Bruker BioSpin), as described previously (Higuchi et al., 2005). Coronal T2-weighted MR images were acquired by three-dimensional (3D) fast spin-echo sequence with the following imaging parameters: echo time = 5.5 ms, repetition time = 3000 ms, RARE factor = 32, field of view (FOV) = 20 × 20 × 25 mm^3, matrix dimensions = 256 × 512 × 60, and nominal resolution = 78 μm × 39 μm × 417 μm. The MRI data were used as an anatomical template for subsequent PET studies.

Radiochemical synthesis. Preparation of [^{11}C]CH_3I for labeling and radiosynthesis of [^{11}C]AC-5216 [*N*-benzyl-*N*-ethyl-2-(7-^{11}C-methyl-8-oxo-2-phenyl-7,8-dihydro-9*H*-purin-9-yl) acetamide] were performed as described previously (Zhang et al., 2007). Briefly, [^{11}C]CO_2 was bubbled into 0.04 M $LiAlH_4$ in anhydrous tetrahydrofuran (300 μl). After evaporation of tetrahydrofuran, the remaining complex was treated with 57% hydroiodic acid (300 μl). [^{11}C]CH_3I was transferred under helium gas flow with heating into a reaction vessel containing 0.6 mg of precursor compound, 4 μl of aqueous NaOH (0.5 N), and 300 μl of anhydrous dimethylformamide cooled to −10 to −15°C. After radioactivity reached a plateau, the reaction vessel was warmed to 30°C and maintained at this temperature for 3 min. The reaction was terminated by adding a solution of CH_3CN and H_2O (6:4, 500 μl), and the radioactive mixture was applied to a semipreparative HPLC system. HPLC purification was completed by the use of a Capcell Pack column (ϕ10 mm × 250 mm; Shiseido) with a mobile phase (CH_3CN:H_2O = 6:4) at a flow rate of 6.0 ml/min. Radioactive fraction corresponding to the desired product was collected in a sterile flask, evaporated to dryness *in vacuo*, redissolved in 10 ml of sterile saline, and passed through a 0.22 μm filter (Millipore) for analysis and animal experiments. The radiochemical purity of the resultant compound was >99%, and its specific radioactivity was 199 ± 72 GBq/μmol at the end of synthesis.

[^{18}F]FEDAA1106 [*N*-(5-fluoro-2-phenoxyphenyl)-*N*-(2-[^{18}F] fluoroethoxy-5-methoxybenzyl)acetamide] was radiosynthesized using its desmethyl precursor, DAA1123, generously provided by Taisho Pharmaceutical, as described previously in detail (Zhang et al., 2004). The radiochemical purity of the end product exceeded 95%, and its specific radioactivity was 255.5 ± 14.8 GBq/μmol (mean ± SD) at the end of synthesis. [^{11}C]PIB [*N*-[^{11}C]methyl-2-(4-methylaminophenyl)-6-hydroxybenzothiazole] for amyloid imaging was synthesized as described previously (Maeda et al., 2007). The radiochemical purity of [^{11}C]PIB was >97%, and its specific radioactivity was 169 ± 37.3 GBq/μmol at the end of synthesis.

In vitro [^{11}C]AC-5216 autoradiography and immunohistochemical and histochemical examinations of tau Tg mouse brains. PS19 mice at 3–17 months of age (n = 21), APP$_{E693\Delta}$ Tg mice at 22–33 months of age (n = 9), and age-matched nTg mice on B6C3H/F1 (n = 15) and C57BL/6 (n = 5) backgrounds deeply anesthetized by excessive dose of pentobarbital (200 mg/kg, i.p) were transcardially perfused with PBS, and then brains were removed. The tissues were fixed with 4% paraformaldehyde overnight, cryoprotected with 20% sucrose in phosphate buffer. Frozen brain samples were cut into 10-μm-thick coronal slices by cryotome (HM560; Carl Zeiss), and the slices were mounted on slide glass (Matsunami Glass) and stored at 4°C pending assays. These sections were reacted with 1 nM [^{11}C]AC-5216 in 50 mM Tris-HCl buffer, pH7.4, at room temperature for 1 h, washed with ice-cold Tris-HCl buffer for 2 min twice, warmly blow-dried, and contacted to an imaging plate (BAS-MS; Fuji Film) for 2 h. The imaging plate data were scanned with a BAS5000 system (Fuji Film).

Slices adjacent to those used for autoradiography were immunostained with mouse monoclonal antibody (AT-8) against phosphorylated tau proteins and chemically stained with a common amyloid dye, thioflavin-S (Wal-

deck) (Yoshiyama et al., 2007). All stained sections were examined with an all-in-one microscope/digital camera (BZ-9000; Keyence). Additional adjacent sections were also doubly immunostained with mouse monoclonal antibody against NeuN and rabbit polyclonal antibody against mouse TSPO (NP155). Areas with AT8 and NeuN immunoreactivities and intensity of TSPO immunoreactivity were estimated in each hippocampal section by Photoshop 7.0 software (Adobe System).

Ex vivo *[^{11}C]AC-5216 autoradiography and histochemical examinations of APP and tau Tg mice. Ex vivo* autoradiographic assessments of regional brain radioactivities were conducted for APP23 and PS19 mice. Animals were given injections of [^{11}C]AC-5216 (37 MBq) into the tail vein under anesthesia with 1.5% (v/v) isoflurane in air (2 ml/min flow rate) and were killed by decapitation at 30 min after the tracer injection. Brains were immediately removed and frozen in powdered dry ice. Frozen brain tissue was coronally cut into 20-μm-thick sections using a HM560 cryotome (Carl Zeiss). Autoradiographic signals were acquired and mapped as in *in vitro* assays.

Following attenuation of radioactivity, brain sections of APP23 mice used for autoradiographic experiments were fixed with 4% paraformaldehyde in PBS for 24 h and stained with 0.01% FSB in 50% ethanol (Sato et al., 2004; Higuchi et al., 2005).

Small animal PET imaging. All PET scans were performed using a microPET Focus 220 animal scanner designed for rodents and small monkeys, which provides 95 transaxial slices 2.0 mm (center-to-center) apart, a 19.0 cm transaxial FOV, and a 7.6 cm axial FOV (Tai et al., 2005). Before the scans, mice were anesthetized with 1.5% (v/v) isoflurane, and a 30-gauge needle connected to a 1 ml polypropylene syringe via a length of polyethylene tubing was inserted into the tail vein. A dynamic emission scan in 3D acquisition mode immediately after intravenous injection of [^{11}C]AC-5216 (38.5 ± 10.1 MBq; specific radioactivity, 140 ± 44.4 at injection) or [^{18}F]FEDAA1106 (30.3 ± 9.29 MBq; specific radioactivity, 197 ± 48 at injection) was performed for 60 or 90 min. All list-mode data were sorted into 3D sinograms, which were then Fourier rebinned into 2D sinograms (frames, 10 × 1, 8 × 5, and 1 × 10 min). Summation images in three time frames (30 min each) after radioligand injection were reconstructed with maximum *a posteriori* (MAP) method, and dynamic images were reconstructed with filtered back-projection using a 0.5 mm Hanning's filter. Volumes of interest (VOIs) were placed on the hippocampus, entorhinal cortex, and striatum using PMOD image analysis software (PMOD Group) with reference to the MRI template. The tracer uptake in each VOI was estimated as percentage of injection dose per unit volume (%ID/ml). We also quantified binding potential (BP_{ND}; ratio at equilibrium of specifically bound radioligand to that of nondisplaceable radioligand in tissue) and distribution volume ratio (DVR; target-to-reference ratio of the distribution volume) for [^{11}C]AC-5216 and [^{18}F]FEDAA1106 in the hippocampus on the basis of a simplified reference tissue model (Lammertsma et al., 1996) and Logan's noninvasive method (Logan et al., 1996), respectively, by using the striatal data as references.

Kinetic properties of [^{11}C]AC-5216 and [^{18}F]FEDAA1106 were analyzed in the same PS19 mice aged 11 months (age = 10.7 ± 0.12 months; $n = 8$), and thereafter compared with those in age-matched nTg mice (age = 11.7 ± 0.77 months; $n = 6$). For the purpose of clarifying the effects of age on the levels of [^{11}C]AC-5216 accumulation in tau Tg mouse brains, the test group was expanded to cover ages ranging from 3 to 14 months, and a total of 45 [^{11}C]AC-5216-PET examinations were performed for 13 nTg and 22 PS19 mice, including 11 individuals receiving two or three scans 2–3 months apart.

We also analyzed the TSPO levels in APP23 mice aged from 23 to 29 months (age = 25.1 ± 1.3 months; $n = 9$), $APP_{E693\Delta}$ mice at 25.4 months of age ($n = 3$), and age-matched nTg mice (age = 25.4 ± 2.60 months; $n = 5$) by the comparative use of [^{11}C]AC-5216 and [^{18}F]FEDAA1106. [^{11}C]PIB-PET scans were also performed for 12 APP23 mice undergoing [^{11}C]AC-5216-PET measurements as described previously in detail (Maeda et al., 2007). Briefly, emission scans were acquired for 60 min in 3D list mode immediately after the intravenous injection of [^{11}C]PIB (30.3 ± 5.5 MBq).

PS19, APP23, and nTg mice prepared for PET analyses were distinct from those used for postmortem *in vitro* autoradiographic and neuropathological assays, while all $APP_{E693\Delta}$ mice undergoing PET scans were incorporated in the postmortem study group.

Statistical analyses. Statistical examinations in the present study were performed using Prism version 5 software (GraphPad Software). For group comparisons of pharmacokinetic variables, we performed either *t*-statistic or ANOVA followed by *post hoc* Bonferroni's test for multiple comparison. Correlations between two variables were evaluated by Pearson product-moment correlation coefficient. Partial correlation coefficient analysis was conducted with SPSS software (SPSS).

Results

Localization of TSPO-immunoreactive microglia in AD and non-AD tauopathy brains

We initially investigated associations of TSPO immunoreactivity with Aβ and tau lesions in autopsied human brains. In AD patients, diffuse plaques, which were only faintly labeled with FSB, were enveloped by a small number of Iba-1-positive microglia, which were negative for TSPO (Fig. 1*A–D*). By contrast, numerous microglia positive for Iba-1 and TSPO were in close contact with neuritic plaques intensely labeled with FSB (Fig. 1*E–H*). Localization of TSPO signals to astrocytes was ruled out by double immunostaining for TSPO and GFAP (Fig. 1*I,J*). Microglia weakly labeled with anti-Iba-1 antibody were also present in control brains, but did not exhibit TSPO immunoreactivity (Fig. 1*K,L*). Iba-1 and TSPO signals were abundantly detected in brains of patients with Pick's disease and PSP enriched with AT8-positive NFTs, Pick's bodies, and neuropil threads (Fig. 1*M–P*). Thus, microglia expressing TSPO were recruited to fibrillar tau inclusions but not Aβ deposits unaccompanied by tau pathologies.

In vivo PET imaging of TSPO in nTg mouse brains by [^{11}C]AC-5216

Before analyses of Tg mice, pharmacokinetic profiles of intravenously administered [^{11}C]AC-5216 in brains of nTg mice aged 7–11 months were assessed by *in vivo* PET (supplemental Fig. 1*A,C*, available at www.jneurosci.org as supplemental material). Images generated by averaging dynamic data from 30 to 90 min indicated that retention of [^{11}C]AC-5216 was highest in the pons/medulla, followed by the cerebellum (supplemental Fig. 1*A*, available at www.jneurosci.org as supplemental material). Radiosignals were relatively low in the hippocampus and neocortex and lowest in the striatum (supplemental Fig. 1*A*, available at www.jneurosci.org as supplemental material). [^{11}C]AC-5216 accumulation in the pons/medulla and cerebellum was markedly abolished by pretreatment with a nonradioactive TSPO ligand, PK11195 (5 mg/kg, i.v.), at 2 min before radiotracer injection (supplemental Fig. 1*B*, available at www.jneurosci.org as supplemental material). The uptake of [^{11}C]AC-5216 in all brain regions peaked at 90 s after injection, and thereafter the decay-corrected radioactivity in the striatum, mostly derived from free and nonspecifically bound tracers, decreased with a half-life of ~25 min (supplemental Fig. 1*C*, available at www.jneurosci.org as supplemental material). The initial uptake of [^{11}C]AC-5216 in all regions was significantly modified by pretreatment with PK11195 [$F_{(25,375)} = 12.7$, $p < 0.05$ (pons/medulla); $F_{(25,375)} = 9.4$, $p < 0.001$ (hippocampus); $F_{(25,375)} = 11.3$, $p < 0.001$ (striatum) for interaction between treatment and time], which is attributable to the blockade of TSPO in blood cells and peripheral organs and consequent elevation of plasma radiotracer concentration. Meanwhile, the retention of [^{11}C]AC-5216 at 60–90 min was significantly suppressed by PK11195 in the pons/medulla ($p < 0.05$ by Bonferroni's test) but not in the hippocampus and striatum ($p > 0.05$ by Bonferroni's test).

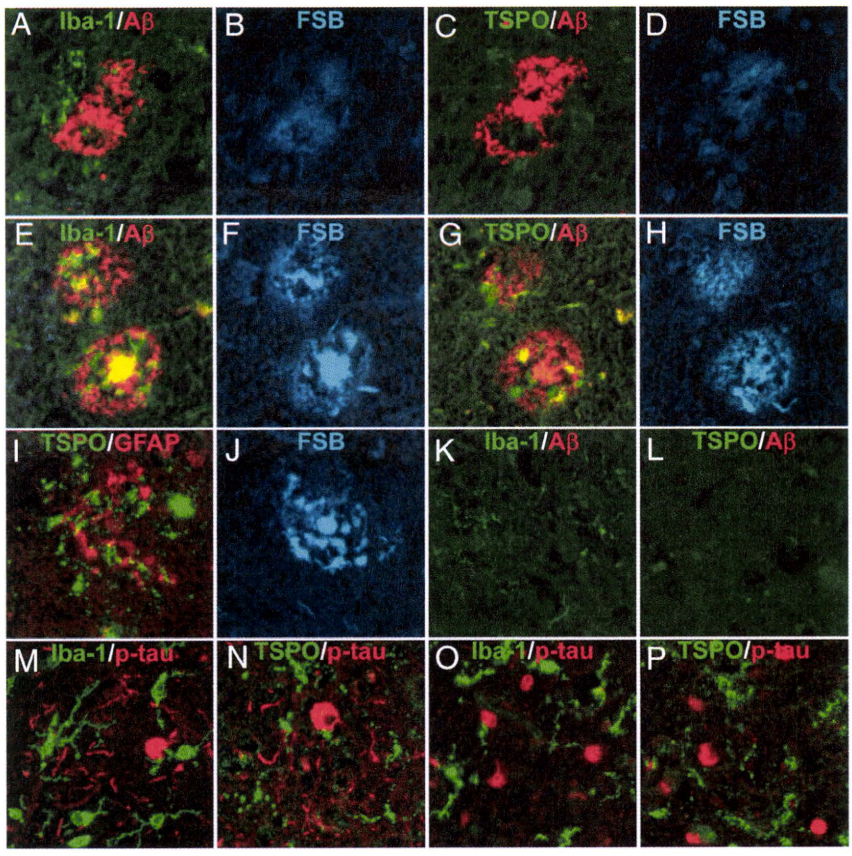

Figure 1. Emergence of TSPO-expressing microglia in AD and non-AD tauopathy brains as assessed by fluorescence microscopy. ***A–D***, Triple labeling of a diffuse plaque in a frontal cortex section of AD brain (***A***, ***B***) and its adjacent slice (***C***, ***D***). The plaque deposition enriched with AβN3pE (red in ***A***, ***C***) was weakly stained with FSB (***B***, ***D***), and induced recruitment of a few Iba-1-immunoreactive microglia (green in ***A***), which were negative for TSPO (green in ***C***). ***E–H***, Double labeling of neuritic plaques in a hippocampal section of AD brain (***E***, ***F***) and its adjacent slice (***G***, ***H***). The AβN3pE-rich plaques (red in ***E***, ***G***) contained dense amyloid cores and dystrophic neurites strongly stained with FSB (***F***, ***H***), and were surrounded by Iba-1 (green in ***E***) and TSPO (green in ***G***) immunoreactivities. ***I***, ***J***, Triple staining of a neuritic plaque in AD hippocampus, showing intense FSB labeling (***J***) and no overlaps between TSPO (green in ***I***) and GFAP (red in ***I***) immunoreactivities. ***K***, ***L***, Double immunostaining of frontal cortex sections generated from a nondemented control brain sample. Resident microglia displayed faint Iba-1 (green in ***K***) but no TSPO (green in ***L***) signals. AβN3pE-positive lesions were barely detectable (red in ***K***, ***L***). ***M–P***, Two-channel fluorescence microscopic views of frontal cortex sections generated from PSP (***M***, ***N***) and Pick's disease (***O***, ***P***) brains. Anti-phospho-tau antibody, AT8, illuminated numerous neuropil threads, NFTs (red in ***M***, ***N***) and Pick's bodies (red in ***O***, ***P***). Iba-1 (green in ***M***, ***O***) and TSPO (green in ***N***, ***P***) immunoreactivities were present in cells with nearly the same morphology, which were characterized as putative microglia.

In vivo PET imaging of neuroinflammation in PS19 mice

MAP reconstruction of microPET data provided high-resolution images illustrating localization of [^{11}C]AC-5216 binding to TSPO in 11-month-old PS19 (Fig. 2*A*) and nTg (Fig. 2*B*) mouse brains. Levels of [^{11}C]AC-5216 signals in the hippocampus and entorhinal cortex of PS19 mice were higher than those of age-matched nTg mice, while there was no overt difference in the striatal radiosignal intensity between these two genotypes. Similar to PET findings, *ex vivo* autoradiographic mapping of [^{11}C]AC-5216 demonstrated that radiotracers intensely accumulated in the hippocampus and entorhinal cortex of PS19 mice relative to nTg controls, which displayed radioactivities primarily in ventricular areas, at 30 min after being intravenously administered (Fig. 2*C*). These data were in line with the spatial extent of tau-induced neuroinflammation and neurodegeneration in PS19 mice clarified in our previous *in vitro* autoradiographic and *in vivo* MRI experiments (Yoshiyama et al., 2007).

Time-radioactivity curves for intracranial kinetics of [^{11}C]AC-5216 also supported elevated TSPO levels in tau-rich regions of PS19 mice ($n = 8$) compared with nTg controls ($n = 6$) (Fig. 3*A*,*B*) in contrast to the similarity of striatal dynamic data between Tg and nTg mice (Fig. 3*C*). The uptake and retention of [^{11}C]AC-5216 estimated as %ID/ml in the striatum of PS19 mice were comparable to those of nTg mice without correction for body weight. Indeed, the area under the curve for PS19 striatum did not differ from nTg control value ($t = 0.22$, $p > 0.05$), despite a notable difference in body weight between these two genotype groups (23.6 g vs 36.8 g, $t = 4.6$, $p < 0.001$). In consideration of changes in body weight disproportionate to brain weight, we presumed %ID/ml to be more suitable than body mass-corrected index for quantifying distribution of this radioligand in the brain.

The difference in retention of [^{11}C]AC-5216 in the hippocampus and entorhinal cortex between PS19 and nTg mice was more explicitly displayed by plotting target-to-striatum ratios of the radioactivity over the scan time [$F_{(1,12)} = 24.9$, $p < 0.001$ (hippocampus); $F_{(1,12)} = 30.5$, $p < 0.001$ (entorhinal cortex) for main effect of genotype] (Fig. 3*D*,*E*). We also determined BP_{ND} for [^{11}C]AC-5216 based on simplified reference tissue model using striatal data as references (Fig. 3*F*). BP_{ND} values were significantly increased in the hippocampus and entorhinal cortex of PS19 mice compared with nTg mice ($F_{(1,24)} = 39.9$, $p < 0.001$ for main effect of genotype).

All eight PS19 mice undergoing [^{11}C]AC-5216-PET received an additional scan with [^{18}F]FEDAA1106 (Fig. 4). Retention of both [^{11}C]AC-5216 (Fig. 4*A*) and [^{18}F]FEDAA1106 (Fig. 4*B*) in the hippocampus exceeded that in the striatum. However, slow clearance of unbound and nonspecifically bound [^{18}F]FEDAA1106 from brain tissues hampered high-contrast detection of specific binding sites (Fig. 4*B*). BP_{ND} for [^{18}F]FEDAA1106 in the hippocampus was intimately correlated with that for [^{11}C]AC-5216 ($r^2 = 0.71$, $p < 0.01$ by Pearson's correlation coefficient), but the detection power of [^{18}F]FEDAA1106 for TSPO increase was approximately half that of [^{11}C]AC-5216, judging from the regression slope in the correlation plot (Fig. 4*C*).

Progressive increase of *in vivo* TSPO signals and their neuropathological correlates in PS19 mice

In an expanded group of PS19 mice, *in vivo* radiolabeling of TSPO with [^{11}C]AC-5216 was quantified in the hippocampus and entorhinal cortex of PS19 and nTg mice at different ages (Fig. 5*A*). Increase of radiotracer retention was also noticeable in the medial frontal cortex, while no overt changes were found in the striatum (Fig. 5*A*). Quantitative measurements of ligand binding in the hippocampus demonstrated no change in BP_{ND} at 3 months of age and significant increase of this index at 7 and 11 months of age relative to age-matched nTg controls ($F_{(2,34)} = 11.2$, $p < 0.001$ for interaction between age and genotype; $p < 0.01$ and $p < 0.001$ at 7 and 11 months of age, respectively, by